

Universal Pansharpener Foundation Model

Hebaixu Wang, Jing Zhang[†], *Senior Member, IEEE*, Haonan Guo, Di Wang, Jiayi Ma[†], *Senior Member, IEEE*,
Bo Du[†], *Senior Member, IEEE*, Liangpei Zhang, *Fellow, IEEE*

Abstract—Pansharpener generates the high-resolution multi-spectral (MS) image by integrating spatial details from a texture-rich panchromatic (PAN) image and spectral attributes from a low-resolution MS image. Existing methods are predominantly satellite-specific and scene-dependent, which severely limits their generalization across heterogeneous sensors and varied scenes, thereby reducing their real-world practicality. To address these challenges, we present FoundPS, a universal pansharpener foundation model for satellite-agnostic and scene-robust fusion. Specifically, we introduce a modality-interleaved transformer that learns band-wise modal specializations to form reversible spectral affine bases, mapping arbitrary-band MS into a unified latent space via tensor multiplication. Building upon this, we construct a latent diffusion bridge model to progressively evolve latent representations, and incorporate bridge posterior sampling to couple latent diffusion with pixel-space observations, enabling stable and controllable fusion. Furthermore, we devise infinite-dimensional pixel-to-latent interaction mechanisms to comprehensively capture the cross-domain dependencies between PAN observations and MS representations, thereby facilitating complementary information fusion. In addition, to support large-scale training and evaluation, we construct a comprehensive pansharpener benchmark, termed PSBench, consisting of worldwide MS and PAN image pairs from multiple satellites across diverse scenes. Extensive experiments demonstrate that FoundPS consistently outperforms state-of-the-art methods, exhibiting superior generalization and robustness across a wide range of pansharpener tasks. Code and models will be publicly released at [FoundPS](#).

Index Terms—pansharpener, large-scale datasets, foundation model, remote sensing.

I. INTRODUCTION

THE substantial demand for high-quality satellite imagery has driven rapid advances in remote sensing systems [1]. Nevertheless, fundamental physical and hardware constraints of satellite sensors prevent the simultaneous acquisition of images possessing both high spatial resolution and rich spectral information [2]. Consequently, most contemporary satellites typically adopt dual-sensor imaging systems, acquiring paired low-resolution multi-spectral (MS) images and high-resolution panchromatic (PAN) images [3]. While MS images provide abundant spectral information across multiple bands at the cost of spatial resolution, PAN images capture fine-grained spatial structures by integrating a broad spectral range into a single channel, albeit with limited spectral diversity. To

H. Wang and J. Ma are with the School of Electronic Information, Wuhan University, Wuhan, China. J. Zhang, D. Wang and B. Du are with the School of Computer Science, Wuhan University, Wuhan, China. H. Guo and L. Zhang are with the State Key Laboratory of Information Engineering in Surveying, Mapping and Remote Sensing, Wuhan University, Wuhan, China. All authors except for L. Zhang are also with the Zhongguancun Academy, Beijing, China. (e-mail: {wanghebaixu, jingzhang.cv, jyma2010}@gmail.com, {haonan.guo, d_wang, dubo, zlp62}@whu.edu.cn).

[†]: Corresponding author.

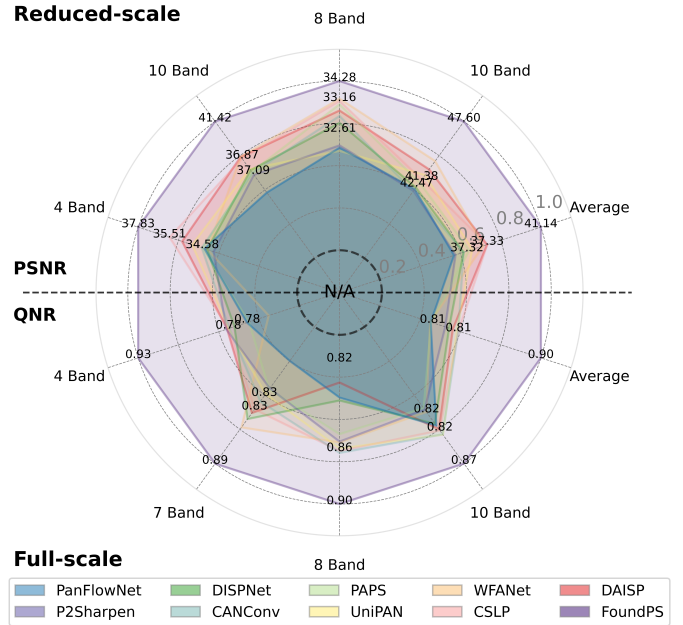


Fig. 1: Pansharpener performance comparisons on PSBench across representative spectral band configurations (4-, 7-, 8-, and 10-band). The upper and lower panels show the reduced- and full-scale evaluations using PSNR and the non-reference QNR metric, respectively. FoundPS consistently outperforms the advanced task-specific models, offering a universal solution for pansharpener tasks.

alleviate this inherent trade-off, pansharpener aims to fuse the complementary information from both modalities, thereby generating images with high spectral fidelity and spatial resolution [4], [5]. Owing to the superior characteristics of fused images, pansharpener has become a critical technique in remote sensing, supporting a wide range of applications across diverse domains [6], [7].

Traditional pansharpener methods are conventionally categorized into three principal families: component substitution (CS) [8], multi-resolution analysis (MRA) [9], [10], and variational optimization (VO) [11], [12], [13]. Generally, they all rely on handcrafted rules or priors to model the relationship between modalities, and operate under the assumption that spectral and spatial information can be effectively separated and recombined. Benefiting from explicit formulations, traditional methods typically allow for straightforward adaptation to MS images with varying numbers of spectral bands. However, their performance is fundamentally constrained by the oversimplified cross-modal fusion assumptions, which suffer from inevitable drawbacks in simultaneously preserving spectral fidelity and enhancing spatial details.

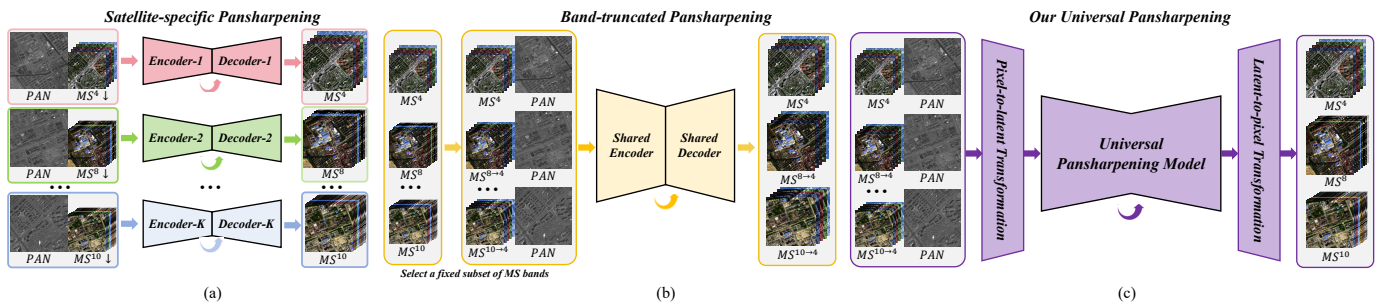


Fig. 2: Mainstream pansharpening paradigms: (a) Satellite-specific methods employ independent encoder–decoder architectures per spectral configuration, resulting in parameter redundancy and poor cross-satellite scalability. (b) Band-truncated methods unify data format by selecting a fixed band subset, enabling joint training but discarding spectral information and losing the ability to process excluded bands. (c) Our universal method performs band-agnostic fusion by projecting arbitrary-band MS images into a shared latent space, achieving unified modeling without band truncation or parameter duplication, while preserving full cross-band and cross-modal information.

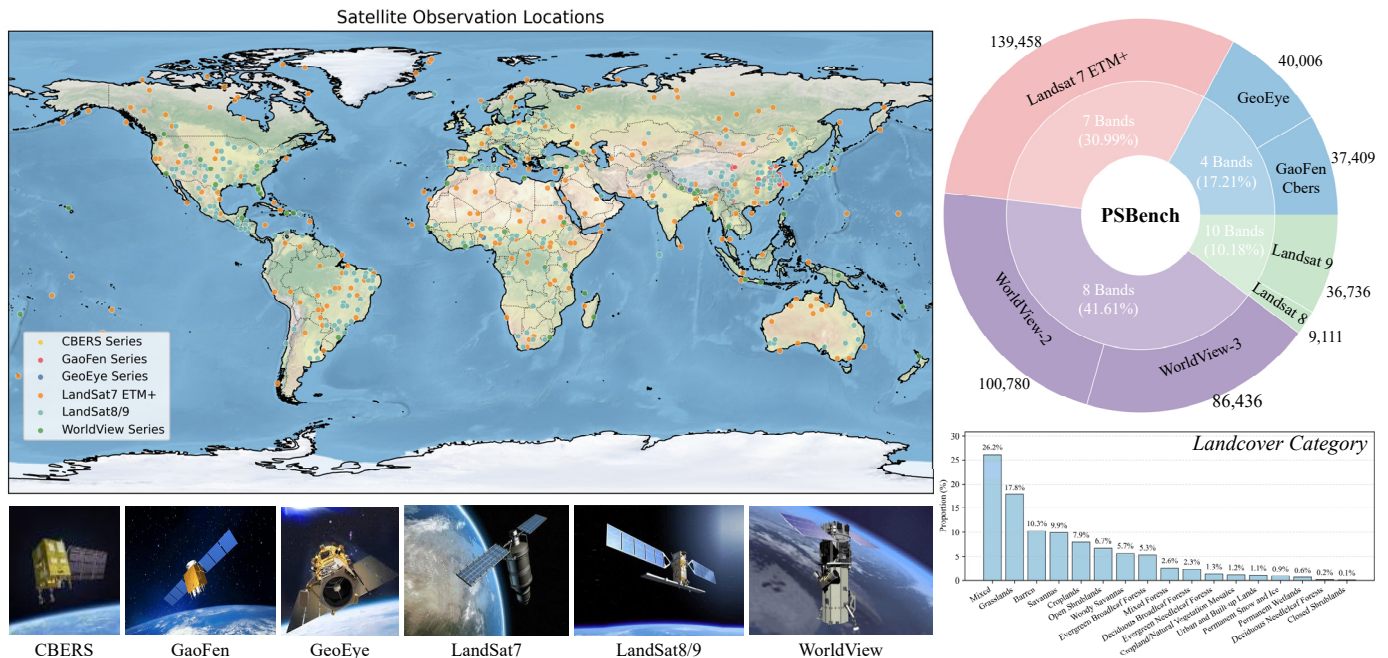


Fig. 3: Satellite observation locations and distribution of PSBench. It contains four representative spectral configurations for pansharpening tasks with over seventeen landcover categories.

So far, the advent of deep learning has led to significant advancements in pansharpening tasks [14]. Existing deep-learning-based methods can be generally classified into two paradigms, as illustrated in Fig. 2. Most approaches adopt independent encoder–decoder architectures built upon convolutional neural networks (CNN) [15], [16], generative adversarial network (GAN) [17], [18], vision transformers (ViT) [19], [20], space state model (SSM) [21], [22], or their hybrid variants. By incorporating sophisticated spectral–spatial interaction mechanisms, these models have substantially achieved improvements in the preservation of both spatial information and spectral fidelity. Nevertheless, these methods remain predominantly satellite-specific, exhibiting limited generalization capabilities across heterogeneous sensors and varying imaging conditions, as shown in Fig. 2(a). Specifically, models trained on fixed spectral band configurations are not applicable to different band settings. Moreover, even under identical band numbers, fusion performance frequently deteriorates when

applied to unseen scenes or incompatible satellite data. To mitigate these limitations, the zero-shot learning paradigm [23], [24], [25] reformulates pansharpening as image-pair-specific fusion tasks, wherein a dedicated model is tailored for each source image pair to inherently accommodate arbitrary spectral dimensionalities. However, it generally yields suboptimal performance without large-scale training. Alternatively, band-truncated pansharpening paradigm [26], [27] attempts to improve cross-sensor generalization by selecting a fixed subset of spectral bands and discarding others to enforce a unified data format, as presented in Fig. 2(b). While this strategy offers improved generalization ability for sensors sharing the selected bands, it fundamentally fails to adapt to the spectral bands that are excluded. In consequence, its applicability is restricted to a narrow range of sensors and scenarios, lacking true universality and compromising the completeness of spectral information. In conclusion, these persistent challenges in cross-sensor generalization and spectral adaptability underscore the urgent

necessity for pansharpening foundation models that trained on massive datasets and optimized with substantial computational resources. Such model could offer the necessary versatility and robustness for universal fusion. However, the advancement towards a truly universal pansharpening foundation model is impeded by three crucial challenges. First, the absence of a unified, band-agnostic modeling paradigm prevents existing methods from accommodating arbitrary spectral configurations, rendering them inherently incompatible with different satellites. As a result, practical deployment requires training and maintaining separate models for individual sensors, severely limiting scalability. Second, current methods often suffer from pronounced performance degradation on unseen scenes and incompatible satellite data due to inherent inductive biases even when applied to matched spectral configurations, indicating limited generalization ability. Third, the lack of worldwide large-scale, multi-sensor datasets further constrains the development and assessment of pansharpening foundation models, as existing datasets are restricted to specific regions and lack geographic diversity.

To address these challenges, we propose **FoundPS**, a universal pansharpening foundation model for satellite-agnostic and scene-robust fusion. Fundamentally, we conceptualize pansharpening into three stages, namely unifying band-agnostic MS representations, enabling effective cross-modality interaction, and restoring desired high-resolution MS images. Firstly, we present a modality-interleaved transformer (MiT) that ensembles mixture-of-experts to generate band-wise modal specializations as a set of spectral affine bases, which are concatenated rather than conventionally weighted aggregation to form reversible mapping matrices. Through tensor multiplication, MS images with arbitrary bands are deterministically projected into a unified latent space, thereby achieving band-agnostic representation with consistent dimensionality. Secondly, we develop the latent diffusion bridge model (LDBM) to progressively evolve the latent representation toward high quality. Furthermore, we incorporate the bridge posterior sampling (BPS) strategy, which tightly couples latent diffusion with pixel observations to provide manifold-constrained fusion guidance. This simultaneously reduces discretization error and shortens the sampling trajectories, and enables training-free adaptation to unseen sensors and scenes, thereby enhancing generalization, thereby enhancing generalization capability. Thirdly, we devise an infinite-dimensional pixel-to-latent interaction mechanism to comprehensively capture the cross-modal dependencies between the pixel-space PAN observation and the latent-space MS representation via Hadamard Product modulated by geometric kernel and exponential kernel, effectively promoting the complementary fusion of spectral and spatial information. In addition, we construct PSBench, a large-scale pansharpening benchmark comprising worldwide MS-PAN image pairs from multiple satellites across diverse geographic scenes (Fig. 3), to support systematic training and evaluation of universal pansharpening models. Extensive experiments demonstrate that FoundPS consistently outperforms state-of-the-art methods (Fig. 1), exhibiting superior generalization capability and robustness across a wide range of pansharpening tasks. Our contributions are summarized below:

- We design a modality-interleaved transformer that generates modal specializations to form spectral affine bases. These bases constitute reversible mapping matrices that deterministically project MS images with arbitrary spectral bands into a unified latent space of fixed dimensionality, enabling band-agnostic representation learning.
- A latent diffusion bridge model equipped with bridge posterior sampling is developed to progressively refine a high-quality representation. This jointly reduces discretization error, accelerates sampling by tightly coupling latent diffusion with pixel observations, and enables training-free adaptation that critically boosts generalization across unseen scenes and satellite data.
- To extremely facilitate the cross-modal dependencies between pixel-space PAN observation and latent-space MS representation, we devise an infinite-dimensional interaction mechanism. It models feature interactions via Hadamard product modulated by a geometric kernel and an exponential kernel, enabling comprehensive complementary fusion of spectral and spatial information.
- We construct PSBench, a large-scale pansharpening benchmark comprising 450K worldwide MS-PAN image pairs from multiple satellites across diverse geographic scenes, to fully support the comprehensive training and evaluation of universal pansharpening foundation models.

The remainder of this paper is organized as follows. In Section II, we introduce the related work and research background. In Section III, we describe the dataset details and methodology of the proposed method. In Section IV, we provide experimental settings and verify the superiority of our method. Conclusions are given in Section V.

II. RELATED WORK

A. Mixture-of-Experts System

Mixture of experts (MoE) [28] framework operates on a simple yet powerful principle that different parts of a model specialize in different tasks or aspects of data [29]. Typically, it consists of multiple feed-forward layers with each serving as an expert, and a gating network that dynamically selects and combines expert outputs. Dense MoE activates all experts and aggregates their outputs to obtain favorable task performance but incurs a significant increase in computational overhead, such as EvoMoE [30], MoLE [31], and DSMoE [32]. In contrast, sparse MoE computes a weighted combination of only the top- k experts selected by the gating network, achieving a balanced trade-off between performance and efficiency [33], [34] and thus becoming the dominant paradigm. Another focal point of MoE is the design of the gating mechanism. Lewis *et al.* [35] introduce the balanced assignment of sparse experts layer to equalize workload across experts, improving individual specialization and model stability. Besides, many studies [36], [28], [37] incorporate an auxiliary loss function to promote a uniform allocation of tokens among experts, thereby enforcing the workload balance. Moreover, Yuan 2.0-M32 [38] proposes an attention router, which efficiently selects the experts. Additionally, PanGu- Σ [39] presents the random routed experts mechanism, which initially routes tokens to a

domain-specific expert group, followed by a random selection within that group. HmoE [40] introduces a heterogeneous MoE framework to address varying token complexities by utilizing different expert networks with diverse capabilities. UniMoE [41] employs modality-specific encoders and a sparse MoE architecture to efficiently handle multiple modalities.

Generally, current MoE primarily utilizes data-specific experts to process inputs with a unified format, and aggregates their outputs via weighted addition. Its potential to handle data across heterogeneous modalities with varying formats remains unexplored. In this work, we extend MoE to adaptively align the representations of MS inputs with varying bands into a unified latent space, thereby enabling universal pansharpening.

B. Traditional Pansharpening Methods

Traditional pansharpening methods are generally categorized into three groups, namely component substitution, multi-resolution analysis, and variational optimization [11]. Classical CS-based methods, including the intensity hue-saturation (IHS) fusion method [42], Brovey transformations [43], and Gram-Schmidt (GS) orthogonalization method [44], typically project source image pairs into a shared domain and substitute spatially enhanced components to improve spatial details. Such linear substitutions are computationally efficient, but often induce spectral distortions. MRA-based methods extract the fine-grained spatial information from PAN image using multi-scale decomposition or filtering operations, and inject the high-frequency components into upsampled MS images to preserve spectral information, such as wavelet-based fusion [9], [45], Laplacian pyramid methods [46], and smoothing filter-based methods [47]. However, their performance is highly sensitive to the choice of decomposition scales and filters, and spectral inconsistencies may still arise in complex scenes. VO-based methods explicitly model the PAN-MS relationship and formulate pansharpening as an inverse problem solved via iterative optimization under handcrafted priors. For instance, P+XS [48] assumes the PAN image to be a linear combination of MS bands. SIRF [49] introduces gradient sparsity as a regularization prior to enhance structural consistency. BAGDC [50] constructs band-adaptive gradient constraints to refine the spatial structures. Despite the strong interpretability, they often require empirical tuning of multiple regularization terms and involve computationally expensive iterative procedures, which can compromise both performance and practical efficiency. Concretely, traditional methods are adaptable to varying spectral bands by tuning hyperparameters, but they are fundamentally constrained by oversimplified fusion assumptions that compromise either spectral or spatial fidelity.

C. Deep Pansharpening Methods

With the powerful non-linear capacity of deep learning, pansharpening has witnessed substantial advancements. PNN [51] devises the first pansharpening network with three simple convolution layers, achieving the superior performance of that time. PanNet [52] incorporates the residual connection to inject spatial information into the resampled spectral information, thereby preserving the spectral distribution as well as spatial

details. Afterwards, lots of sophisticated structures [53], [54], [55] are investigated to fully explore the nonlinear capacity of the network for superior pansharpening quality [5], [56], [57], [58], [59]. Inspired by the conventional techniques, Hu *et al.* [60] built a multi-scale network to dynamically and locally extract the information from source images. Yang *et al.* [61] embedded a denoising-based prior and a non-local auto-regression prior to improve the long-range coherence, and combined the merits of model optimization with deep learning. Particularly, Ma *et al.* [62] took the first attempt to utilize the generative adversarial network for unsupervised pansharpening paradigm. Multiple discriminators are introduced to assist the generator in jointly learning the reasonable spectral and spatial distributions [17], [63]. ZeroSharpen [23] and ZSPan [25] break the satellite-specific learning paradigm and explore the image-pair-specific fusion strategies to improve the practicality of deep models when processing the insufficient and unknown data. Recent efforts have increasingly focused on improving the fusion generalization across heterogeneous satellites and diverse scenes. Some works [27] employ a band-truncation strategy to enforce a unified input format by selecting a fixed subset of spectral bands and discarding others, thereby enabling models to be optimized on samples from different satellites. UniPAN [26] further projects these standardized data into a shared distribution, reducing the learning difficulty of the network and improving the cross-task adaptability. Additionally, Cui *et al.* [64] simulate datasets for pansharpening pre-training, boosting the generalization capacity.

In summary, existing methods are incapable of handling MS inputs with varying spectral configurations from different satellites, rendering them sensor-specific and non-transferable. And the lack of large-scale, real-world datasets further constrains generalization across diverse scenes. To the best of our knowledge, FoundPS is the first foundation model designed for truly universal pansharpening. Besides, PSBench is the first worldwide, multi-satellite, large-scale benchmark specifically constructed to support the development of pansharpening.

III. METHODOLOGY

A. Data Source

In the light of significant criteria including task diversity, satellite sensors, global coverage, and data accessibility, we select five series of representative satellites to serve as the data sources, as reported in Tab. I. Specifically, to ensure task diversity, we consider pansharpening scenarios involving four, seven, eight, and ten spectral bands configurations, with each exhibiting distinct band orders and spectral ranges. These scenarios present widely varying spatial resolutions, ranging from submeter to tens of meters, and cover spectral wavelengths from visible to thermal infrared, thereby constructing a highly heterogeneous imaging environment. Temporally, the data span from 1999 to 2025, covering multiple generations of satellite sensors. Geographically, samples are globally distributed across seventeen classical land-cover categories, en-

¹<https://data.cresda.cn>

²<https://maxar-opendata.s3.amazonaws.com/>

³<https://www.usgs.gov/landsat-missions/>

TABLE I: Details of the collected multi-spectral and panchromatic image pairs from different satellites.

Satellite Name	Launch Date	Launch Country	MS Spatial Resolution	PAN Spatial Resolution	Multi-Spectral Range	Panchromatic Range	Number of MS Bands	Order of MS Bands	MS Pixel Size	PAN Pixel Size
GaoFen-1 ¹	2013	China	8.0 m	2.0 m	450-890 nm	450-890 nm	4	B/G/R/NIR	256	1024
GaoFen-2 ¹	2014	China	3.2 m	0.8 m	450-890 nm	450-890 nm	4	B/G/R/NIR	256	1024
GaoFen-6 ¹	2018	China	8.0 m	2.0 m	450-900 nm	450-900 nm	4	B/G/R/NIR	256	1024
GaoFen-7 ¹	2020	China	0.65 m	2.6 m	450-890 nm	450-900 nm	4	B/G/R/NIR	256	1024
GeoEye-1 ²	2008	USA	1.64 m	0.41m	450-920 nm	450-900 nm	4	B/G/R/NIR	256	1024
CBERS-04A ¹	2019	China	8.0 m	2.0 m	450-890 nm	450-900 nm	4	B/G/R/NIR	256	1024
Landsat7 ETM+ ³	1999	USA	30 m	15m	450-12500 nm	520-900 nm	7	B/G/R/NIR/SWIR/TIR/MIR	512	1024
WorldView-2 ²	2007	USA	1.84 m	0.46 m	400-1040 nm	450-800 nm	8	C/B/G/Y/R/RE/NIR1/NIR2	256	1024
WorldView-3 ²	2009	USA	1.24 m	0.31 m	400-1040 nm	450-800 nm	8	C/B/G/Y/R/RE/NIR1/NIR2	256	1024
Landsat8 ³	2013	USA	30 m	15 m	430-12510 nm	500-680 nm	10	CA/B/G/R/NIR/SWIR1/SWIR2/Cirrus/TIR1/TIR2	512	1024
Landsat9 ³	2021	USA	30 m	15 m	430-12510 nm	500-680 nm	10	CA/B/G/R/NIR/SWIR1/SWIR2/Cirrus/TIR1/TIR2	512	1024

Band abbreviation: **B**: Blue, **G**: Green, **R**: Red, **NIR**: Near-infrared, **CB**: Coastal Blue, **Y**: Yellow, **RE**: Red Edge, **SWIR**: Short-wave Infrared, **TIR**: Thermal, **CA**: Coastal Aerosol.

suring broad environmental and scene diversity, as illustrated in Fig. 3. Moreover, the benchmark incorporates both freely accessible and commercial satellite data, balancing openness with data quality to support reproducible yet practical research. In this context, these criteria are designed to challenge and enable a foundation model to handle pansharpening tasks under varying spectral configurations and scene complexities. All data utilized in this work have been properly licensed.

B. Data Acquisition and Processing

We collect the source image pairs from both open-access platforms and commercial satellite providers to ensure data quality and diversity. To maintain atmospheric clarity, only samples with cloud and haze coverage below 5% are retained, while all others are discarded. Additionally, we crop all PAN images to 1024×1024 patches, then crop the corresponding MS image according to the precise spatial ratio. To enable supervised training and evaluation, we simulate the reduced-scale MS/PAN image pairs following the Wald’s protocol [65]. This pipeline yields PSBench, a large-scale, globally-covered pan-sharpening dataset comprising 449,936 aligned MS/PAN patch pairs with a total of 1.68 TB, as presented in Fig. 3. For evaluation, we randomly select 1091, 463, 561, and 1029 image pairs from the entire PSBench dataset as test sets for the 4-, 7-, 8-, and 10-band pansharpening tasks, respectively.

C. Method Overview

FoundPS conceptualizes pansharpening into three fundamental stages: unified representation, fusion, and reconstruction, as illustrated in Fig. 4. First, the MS image is upsampled to align its spatial resolution with the PAN image, and then fed into the modality-interleaved transformer. It undergoes band-wise patchification and patch-wise embedding, followed by self-attention and pooling to obtain hidden states, which are then input into the mixture-of-expert system. A router generates probability weights over experts, and a subset of experts corresponding to the number of MS bands is dynamically selected. The selected expert outputs, representing spectral affine bases, are normalized and concatenated to form a reversible mapping tensor. Through tensor multiplication, MS images with arbitrary bands are deterministically projected into a unified latent space, thereby achieving band-agnostic representation with consistent dimensionality. Second, the

initially obtained latent representations are refined through a latent diffusion bridge model, which iteratively evolves them toward higher quality. To enable deep cross-modal fusion, an infinite-dimensional feature interaction mechanism is incorporated, comprehensively integrating PAN features with the evolving latent MS representations. During diffusion inference, we seamlessly integrate bridge posterior sampling strategy, which provides manifold-constrained gradients to guide the fusion process without extra computational overhead. This not only enhances representation quality but also allows training-free fusion adaptation across different satellites and scenes, significantly improving model universality. Finally, the refined latent MS representation is projected back to the image space via the inverse of the mapping tensor, thereby reconstructing the desired high-resolution MS image.

D. Modality-interleaved Transformer

For the first vital stage, we introduce a modality-interleaved transformer to map MS images with arbitrary spectral bands or orders into a band-agnostic unified latent space. Let $x \in \mathbb{R}^{h \times w \times B}$ denote the B -band MS image with a height of h and a width of w . The upsampled MS image is defined as $x \uparrow \in \mathbb{R}^{H \times W \times B}$, which matches the spatial resolution of PAN image $P \in \mathbb{R}^{H \times W \times 1}$ with size of H and W . MiT takes $x \uparrow$ as input and performs band-wise patchification by independently dividing each band into non-overlapping patches. All patches are then embedded to obtain patch embedding $E \in \mathbb{R}^{N \times p^2}$:

$$E = \text{PatchEmbed}(x \uparrow), \tag{1}$$

where $N = B \times \frac{H}{p} \times \frac{W}{p}$ is the number of patches with size p . These patch embeddings are augmented with positional encodings and then processed by a Transformer-based self-attention [66] mechanism to extract hidden states $H \in \mathbb{R}^{N \times p^2}$:

$$H = \text{softmax}\left(\frac{EE^T}{\sqrt{d_k}}\right)E, \tag{2}$$

To aggregate band-wise features and produce a compact representation for expert routing, we employ a query-cached attention pooling mechanism. A learnable query vector $q \in \mathbb{R}^{p^2}$ is replicated to form a query matrix $Q \in \mathbb{R}^{N \times p^2}$, which interacts with the hidden states via cross-attention:

$$H_p = Q + \text{softmax}\left(\frac{QH^T}{\sqrt{d_k}}\right)H. \tag{3}$$

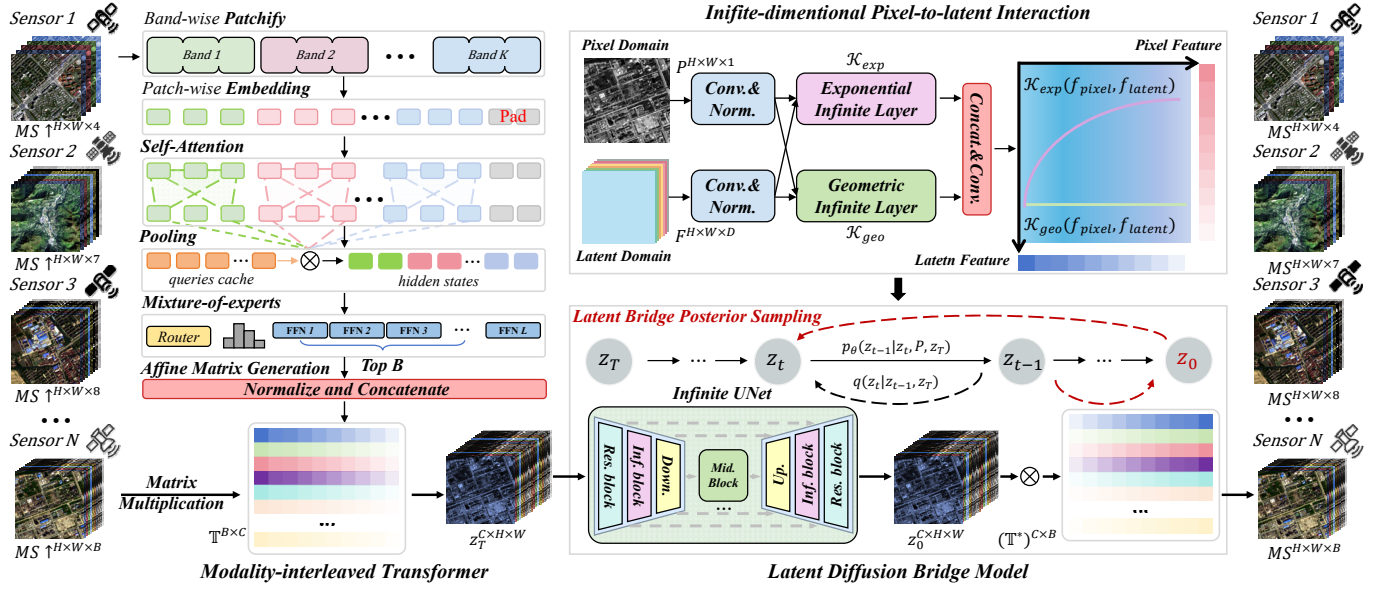


Fig. 4: The overall framework of the proposed FoundPS.

Furthermore, $H_p \in \mathbb{R}^{N \times p^2}$ is condensed into a compact vector $h_p \in \mathbb{R}^{p^2}$ via a summation over the first dimension. Then h_p is fed into a router network \mathcal{G} to produce scores over total L experts and determine a top- B expert cache Ω_B :

$$\Omega_B = \text{TopB}(\text{softmax}(\mathcal{G}(h_p))). \quad (4)$$

Afterwards, the selected experts are activated. Each expert \mathcal{E}_i outputs a spectral affine basis $T_i \in \mathbb{R}^{1 \times C}$. These bases are concatenated to form a reversible mapping tensor $\mathbb{T} \in \mathbb{R}^{B \times C}$, which can be formulated as:

$$\mathbb{T} = [T_1 || T_2 || \dots || T_B], T_i = \mathcal{E}_i(H), i \in \Omega_B. \quad (5)$$

To maintain stability and invertibility, we replace the leading $B \times B$ block of \mathbb{T} with the identity matrix, ensuring well-posed projection while preserving the learned spectral transformations. The arbitrary-band MS image can be projected into a latent representation $\mathbf{Z} \in \mathbb{R}^{H \times W \times C}$ with fixed dimensionality C via tensor multiplication \otimes :

$$\mathbf{Z} = (x \uparrow) \otimes \mathbb{T}, \quad (6)$$

This design ensures that MiT is inherently band-agnostic and provides a consistent latent space for subsequent fusion stages.

E. Latent Diffusion Bridge Model

Diffusion bridge models establish probabilistic paths between arbitrary paired distributions [67]. Here, we leverage this framework to bridge the low-quality representation $\mathbf{z}_T \in p_{LQ}(\mathbf{Z})$ and the high-quality representation $\mathbf{z}_0 \in p_{HQ}(\mathbf{Z})$ in the latent domain, termed the LDBM. Let \mathbf{z}_t be a finite random variable governed by the generalized diffusion bridge process in [68], with terminal condition \mathbf{z}_T . The evolution of its marginal distribution $p(\mathbf{z}_t | \mathbf{z}_T)$ satisfies the following stochastic differential equation under a fixed stationary coefficient ratio λ with noise schedule θ_t (detailed in Apps. A):

$$d\mathbf{z}_t = \theta_t \coth(\bar{\theta}_{t:T})(\mathbf{z}_T - \mathbf{z}_t)dt + \sqrt{2\lambda\theta_t}d\omega_t, \quad (7)$$

where $\bar{\theta}_{s:t} = \int_s^t \theta_\tau d\tau$ and ω_t is the standard Wiener process. Given an initial state \mathbf{z}_0 , the analytical solution of \mathbf{z}_t at time $0 < t < T$ of that SDE in Eq. (7) can be formulated as:

$$\mathbf{z}_t = \mathbf{z}_T + (\mathbf{z}_0 - \mathbf{z}_T) \frac{\sinh(\bar{\theta}_{t:T})}{\sinh(\bar{\theta}_{0:T})} + \int_0^t \sqrt{2\lambda\theta_s} \frac{\sinh(\bar{\theta}_{t:T})}{\sinh(\bar{\theta}_{s:T})} d\omega_s, \quad (8)$$

which satisfies a Gaussian distribution with expectation $\mathbb{E}[\mathbf{z}_t]$ and variance $\text{Var}[\mathbf{z}_t]$:

$$\mathbb{E}[\mathbf{z}_t] = \mathbf{z}_T + (\mathbf{z}_0 - \mathbf{z}_T) \frac{\sinh(\bar{\theta}_{t:T})}{\sinh(\bar{\theta}_{0:T})} := \mathbf{z}_T + (\mathbf{z}_0 - \mathbf{z}_T)\Theta_t, \quad (9)$$

$$\text{Var}[\mathbf{z}_t] = 2\lambda \frac{\sinh(\bar{\theta}_{0:t}) \sinh(\bar{\theta}_{t:T})}{\sinh(\bar{\theta}_{0:T})} := \Sigma_t^2. \quad (10)$$

Apparently, the initial state at $t = 0$ is a high-quality representation \mathbf{z}_0 , while the terminal state at $t = T$ is a low-quality representation \mathbf{z}_T . From Eq. (9)-(10), the transition probability distributions from \mathbf{z}_0 to intermediate states \mathbf{z}_t and \mathbf{z}_{t-1} are:

$$q(\mathbf{z}_t | \mathbf{z}_0, \mathbf{z}_T) = \mathcal{N}(\mathbf{z}_T + (\mathbf{z}_0 - \mathbf{z}_T)\Theta_t, \Sigma_t^2 \mathbf{I}), \quad (11)$$

$$q(\mathbf{z}_{t-1} | \mathbf{z}_0, \mathbf{z}_T) = \mathcal{N}(\mathbf{z}_T + (\mathbf{z}_0 - \mathbf{z}_T)\Theta_{t-1}, \Sigma_{t-1}^2 \mathbf{I}), \quad (12)$$

where \mathbf{I} is standard Gaussian noise. Supposing that sampling from \mathbf{z}_t to \mathbf{z}_{t-1} follows the Gaussian distribution, the deterministic sampling of the reverse process is:

$$\mathbf{z}_{t-1} = \mathbf{z}_T + \frac{\Sigma_{t-1}}{\Sigma_t}(\mathbf{z}_t - \mathbf{z}_T) + (\Theta_{t-1} - \Theta_t \frac{\Sigma_{t-1}}{\Sigma_t})(\hat{\mathbf{z}}_0^t - \mathbf{z}_T), \quad (13)$$

$$= \mathbf{z}_T + \frac{\Theta_{t-1}}{\Theta_t}(\mathbf{z}_t - \mathbf{z}_T) - (\frac{\Theta_{t-1}}{\Theta_t} \Sigma_t - \Sigma_{t-1})\hat{\epsilon}_t, \quad (14)$$

where $\hat{\mathbf{z}}_0^t$ and $\hat{\epsilon}_t$ are the high-quality representation and noise at a certain state predicted by network $\mathcal{U}(z_t, z_T, P, t)$, respectively. Essentially, these two prediction modes are equivalent.

F. Bridge Posterior Sampling

Tweedie's formulas [69] unveil that ϵ_t -prediction is equivalent to estimating the score function, i.e., the gradient of the

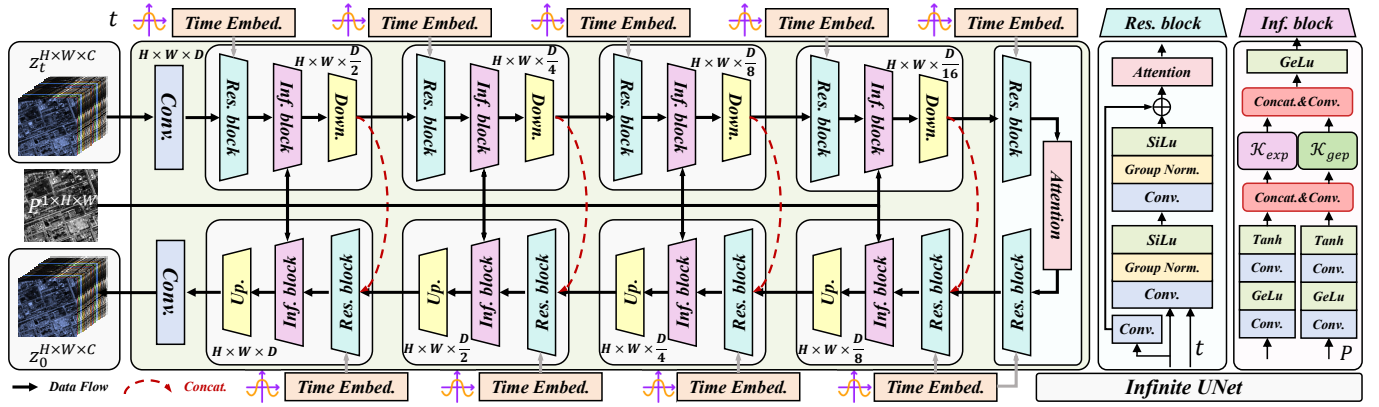


Fig. 5: The network architecture of Infinite-UNet in latent diffusion bridge model.

log-density of the data distribution. For the case of LDBM sampling, $\hat{\epsilon}_t$ in Eq. (14) can be converted into:

$$\hat{\epsilon}_t = -\sum_t \nabla_{\mathbf{z}_t} \log p(\mathbf{z}_t | \mathbf{z}_T). \quad (15)$$

Under such circumstances, we can further incorporate the *Bayer's theorem* to achieve diffusion guidance:

$$\nabla_{\mathbf{z}_t} \log p(\mathbf{z}_t | \mathbf{z}_T) = \nabla_{\mathbf{z}_t} \log p(\mathbf{z}_t) + \nabla_{\mathbf{z}_t} \log p(\mathbf{z}_T | \mathbf{z}_t). \quad (16)$$

Eq. (16) offers profound insights that $\nabla_{\mathbf{z}_t} \log p(\mathbf{z}_T | \mathbf{z}_t)$ can be adapted to prevent samples from deviating from the generative manifolds. However, the likelihood term is in fact analytically intractable due to its dependence on time t . To circumvent the intractability, we use the surrogate function to maximize the likelihood, yielding approximate posterior sampling [70]. Specifically, we make the approximation (see Apps. B):

$$\nabla_{\mathbf{z}_t} \log p(\mathbf{z}_T | \mathbf{z}_t) \approx \nabla_{\mathbf{z}_t} \log p(\mathbf{z}_T | \hat{\mathbf{z}}_0^t), \quad (17)$$

where $\hat{\mathbf{z}}_0^t = \mathbb{E}[\mathbf{z}_0 | \mathbf{z}_T]$ is the estimated high-quality latent representation at time t . Unfortunately, \mathbf{z}_0 and \mathbf{z}_T , as the two endpoints of the latent diffusion bridge, exhibit a weak conditional relationship in the latent space. However, they can be projected back to the pixel space through the invertible tensor matrix \mathbb{T} , which allows us to reformulate the guidance objective. Mathematically, pansharpening can be viewed as a special case of linear inverse problems for multi-spectral imagery, where a degraded MS measurement x is derived from the desired MS image $y \in \mathbb{R}^{H \times W \times B}$ by below formulation:

$$x = y \downarrow + \mathbf{n}, \quad (18)$$

where \downarrow is the forward operator for spatial degradation and \mathbf{n} is the noise. By combining with Eq. (6), we can obtain:

$$\mathbf{z}_T = \mathbb{T}(\mathbb{T}^* \mathbf{z}_0 \downarrow + \mathbf{n}), \quad (19)$$

where \mathbb{T}^* is the inverse of \mathbb{T} . Suppose $(\mathbb{T}\mathbf{n}) \sim \mathcal{N}(0, \sigma^2)$ is Gaussian distribution, then Eq. (17) can be converted to:

$$\nabla_{\mathbf{z}_t} \log p(\mathbf{z}_T | \hat{\mathbf{z}}_0^t) = -1/\sigma^2 \nabla_{\mathbf{z}_t} \|\mathbf{z}_T - \mathbb{T}(\mathbb{T}^* \hat{\mathbf{z}}_0^t \downarrow)\|_2. \quad (20)$$

Furthermore, we can derive the closed-form upper bound of the Jensen gap for the approximation in Eq. (17):

$$\mathcal{J}(\sigma, M) \leq \frac{d}{\sqrt{2\pi}\sigma^2} \exp\left(-\frac{1}{2\sigma^2}\right) \|\nabla_{\mathbf{z}_t} \mathbb{T}(\mathbb{T}^* \hat{\mathbf{z}}_0^t \downarrow)\|_2 M, \quad (21)$$

where $M := \int \|\mathbb{T}^* \mathbf{z}_0 \downarrow - \mathbb{T}^* \hat{\mathbf{z}}_0^t \downarrow\| dp(\mathbf{z}_0 | \mathbf{z}_t)$. Note that M is finite for most of the distribution in practice, which can be considered as the generalized absolute distance between the observed reference and estimated data. $\mathcal{J}(\sigma, M)$ can approach 0 as $\sigma \rightarrow 0$ or ∞ , suggesting that the approximation errors reduce when the measurement noise is extremely small or large. Specifically, if the predictions of $\hat{\mathbf{z}}_0^t$ are accurate, the upper bound $\mathcal{J}(\sigma, M)|_{\sigma \rightarrow 0, M \rightarrow 0}$ shrinks due to the low variance and distortion. Oppositely, if the predictions lack accuracy, the upper bound of the $\mathcal{J}(\sigma, M)|_{\sigma \rightarrow \infty, M \rightarrow M_{max}}$ shrinks as well for large variance and limited distortion. For the inverse inference in Eq. (14), we can employ bridge posterior sampling to guide the current state by the following modifications:

$$\hat{\mathbf{z}}_0^t := \hat{\mathbf{z}}_0^t + \eta_z \nabla_{\mathbf{z}_t} \|\mathbf{z}_T - \mathbb{T}(\mathbb{T}^* \hat{\mathbf{z}}_0^t \downarrow)\|_2, \quad (22)$$

$$\hat{\epsilon}_t := \hat{\epsilon}_t + \eta_\epsilon \nabla_{\mathbf{z}_t} \|\mathbf{z}_T - \mathbb{T}(\mathbb{T}^* \mathbf{z}_0 \downarrow)\|_2. \quad (23)$$

Building on these theoretical foundations, BPS functions as a training-free guidance mechanism that enables flexible control over the fusion effect via a tunable weight $\eta(\cdot)$. Larger values enforce stricter spectral consistency with the MS observation, whereas smaller values preserve more spatial priors, leading to improved structural details. Such a mechanism allows the model to adapt across varying satellite sensors and diverse scenarios, achieving scene-adaptive fusion without retraining. Notably, according to the manifold assumption [71], image data should lie on a low-dimensional manifold, whereas noised quantities do not. Therefore, we adopt the $\hat{\mathbf{z}}_0^t$ -prediction mode as training and sampling criterion, and the corresponding algorithms are detailed in Alg. 1 and Alg. 2, respectively.

G. Infinite Dimension Interaction Block

To progressively refine the latent representation toward high-quality reconstruction, it is crucial to effectively exploit the pixel-domain PAN image as a spatial prior for latent enhancement. However, the inherent domain mismatch between pixel-space PAN features and latent-space MS representations necessitates a principled cross-domain interaction mechanism to enable effective information transfer.

Suppose the feature basis of pixel space to be $\mathcal{A} = \{\alpha_i\}_{i=1}^m$ and that of latent space be $\mathcal{B} = \{\beta_j\}_{j=1}^n$ with degrees of freedom m and n , respectively. Most methods simply

Algorithm 1: FoundPS: Training

Input: MS image x ; PAN image P ; Reference y

repeat

- $\mathbb{T}, P_k, f_k = \mathcal{M}(x \uparrow)$
- $\mathbf{z}_T = \mathbb{T} \otimes x \uparrow$
- $\mathbf{z}_0 = \mathbb{T} \otimes y$
- $t \sim \text{Uniform}(1, \dots, T)$;
- $\epsilon \sim \mathcal{N}(0, \mathbf{I})$;
- $\mathbf{z}_t = \mathbf{z}_T + (\mathbf{z}_0 - \mathbf{z}_T)\Theta_t + \Sigma_t \epsilon$;
- $\hat{\mathbf{z}}_0^t = \mathcal{U}(z_t, z_T, P, t)$
- Take the gradient descent step on
- $\nabla(\|\hat{\mathbf{z}}_0^t - \mathbb{T} \otimes y\|_1 + \|\mathbb{T}^* \otimes \hat{\mathbf{z}}_0^t - y\| + \gamma \sum_{k=1}^K P_k \cdot f_k)$

until converged;

concatenate them to construct the union space $S^{(1)} = \mathcal{A} \oplus \mathcal{B} = \text{span}\{\alpha_1, \dots, \alpha_m, \beta_1, \dots, \beta_n\}$ with the degree of freedom of $d = m + n$. Some of them subsequently devise complicated networks to enrich interactions, while others leverage specific operators to induce higher-order couplings. For instance, star operation [72] utilizes the Hadamard product \odot to extend the feature interaction into an implicit interactive quadratic space $S^{(2)} = W^T \mathcal{V} \odot W^T \mathcal{V} = \text{span}\{\alpha_i \alpha_j, \alpha_i \beta_j, \dots, \beta_i \beta_j\}$ with a degree of freedom $d(d+1)/2$ for $\mathcal{V} \in S^{(1)}$. Self-attention mechanism in Transformers can be viewed as applying two successive Hadamard products among query, key, and value features, which implicitly constructs a cubic interaction space $S^{(3)}$ with a degree of freedom $d(d+1)(d+2)/6$. Generally, for a k -order Hadamard product interaction on features of total dimension d , the dimension of the feature interaction space is:

$$\dim(S^{(k)}) = \binom{d+k-1}{k} = \frac{(d+k-1)!}{(d-1)!k!} \quad (24)$$

To fully exploit feature interactions, we aim to incorporate all orders of interactions by constructing the infinite-dimensional union space:

$$S^{\text{inf}} = S^{(1)} \oplus S^{(2)} \oplus \dots \oplus S^{(\infty)} = \bigoplus_{k=1}^{\infty} S^{(k)}, \quad (25)$$

where \oplus denotes the direct sum of non-redundant components. Intuitively, a naive approach to realizing S^{inf} would require explicitly computing and aggregating infinitely many Hadamard products, which is clearly computationally intractable. Instead, we introduce a geometric surrogate function $\mathcal{K}_{\text{geo}}(\cdot)$ and an exponential surrogate function $\mathcal{K}_{\text{exp}}(\cdot)$. Let $\mathcal{V} \in S^{(1)}$ be a feature representation, then these surrogate functions can implicitly capture and aggregate infinite-order interactions:

$$\mathcal{K}_{\text{geo}}(W^T \mathcal{V}) = \frac{1}{1 - (W^T \mathcal{V})} = \sum_{k=0}^{\infty} (W^T \mathcal{V})^{\odot k}, \quad (26)$$

$$\mathcal{K}_{\text{exp}}(W^T \mathcal{V}) = \exp(W^T \mathcal{V}) = \sum_{k=0}^{\infty} \frac{(W^T \mathcal{V})^{\odot k}}{k!}, \quad (27)$$

where $(\cdot)^{\odot k}$ denotes the k -fold Hadamard power and W^T is a weight matrix that can be densely or sparsely simulated via a linear layer or a convolution layer, respectively. These expansions generate the complete set of all symmetric monomials

Algorithm 2: FoundPS: Sampling

Input: MS image x ; PAN image P ;
network $\mathcal{M}(\cdot), \mathcal{U}(\cdot)$;
guidance weight η .

$\mathbb{T} = \mathcal{M}(x \uparrow)$

$\mathbf{z}_T = \mathbb{T} \otimes x \uparrow$

for $t = T - 1$ to 1 **do**

- $\hat{\mathbf{z}}_0^t = \mathcal{U}(z_t, z_T, P, t)$
- $\mathbf{z}_{t-1} = \mathbf{z}_T + \frac{\Sigma_{t-1}}{\Sigma_t} (\mathbf{z}_t - \mathbf{z}_T) + (\Theta_{t-1} - \Theta_t \frac{\Sigma_{t-1}}{\Sigma_t}) (\hat{\mathbf{z}}_0^t - \mathbf{z}_T)$
- $\hat{\mathbf{z}}_{t-1} = \mathbf{z}_{t-1} + \eta_z \nabla_{\mathbf{z}_t} \|\mathbf{z}_T - \mathbb{T}(\mathbb{T}^* \mathbf{z}_0 \downarrow)\|_2$

end

$\hat{y} = \mathbb{T}^* \otimes \hat{\mathbf{z}}_0$

Output: \hat{y}

spanning S^∞ . Notably, \mathcal{K}_{geo} assigns equal weight to all interaction orders, while \mathcal{K}_{exp} imposes factorial decay on higher-order terms, effectively emphasizing lower-order interactions. Both of them enable the full-order feature interactions, without explicit order selection or truncation.

H. Network Architecture

Our architecture comprises the modality-interleaved transformer and the latent diffusion bridge model. Specifically, MiT comprises a router network and a set of feed-forward expert layers. The former integrates a patch-embedding module, a multi-layer Transformer stack, and a query-cached attention pooling mechanism, followed by a multi-layer perception (MLP) head that produces expert selection scores. The latter consists of multiple parallel sub-networks, each implemented as a lightweight two-layer MLP with gated activation functions, enabling band-wise modal specialization. LDBM adopts a U-Net-shaped denoising architecture with symmetric encoder-decoder layers and skip connections, termed Infinite-UNet, as presented in Fig. 5. Initially, it utilizes a convolutional layer to project input into a D -dimension feature space. Then it employs time-conditioned residual blocks modulated by sinusoidal embeddings to enable step-wise feature adaptation along the diffusion trajectory. To capture long-range dependencies, linear attention and standard self-attention modules are interleaved across scales. Moreover, infinite dimension interaction blocks are inserted at each stage, leveraging geometric-series and exponential-series kernels to model full-order interactions between PAN observation and latent MS features. Additionally, multi-scale representation is learned via strided convolutions in encoder and up-sampling followed by convolution in decoder, maintaining spatial alignment throughout.

I. Loss Functions

To stabilize the fusion performance, we employ a coupled loss that enforces cross-domain consistency by jointly constraining the latent representation and the reconstructed image. Specifically, given the predicted high-quality latent representations $\hat{\mathbf{z}}_0^t$ at time t , the loss is formulated as:

$$\mathcal{L}_{\text{ref}} = \|\hat{\mathbf{z}}_0^t - \mathbb{T} \otimes y\|_1 + \|\mathbb{T}^* \otimes \hat{\mathbf{z}}_0^t - y\|_1, \quad (28)$$

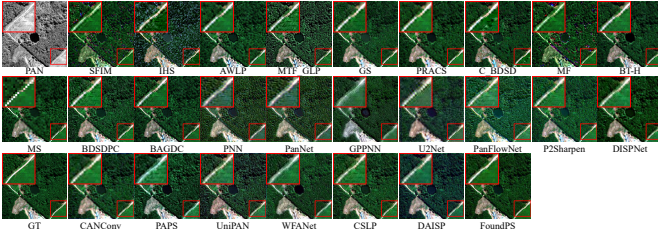


Fig. 6: 4-band visual comparisons of reduced scale on PSBench.

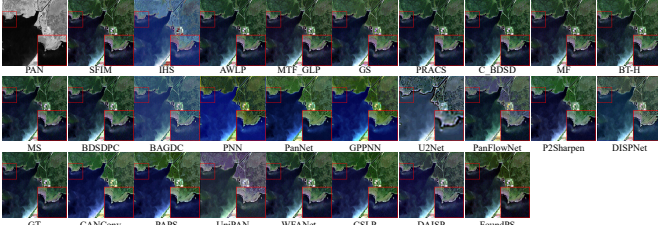


Fig. 7: 7-band visual comparisons of reduced scale on PSBench.

where $\|\cdot\|_1$ represents ℓ_1 loss. In addition, to encourage balanced expert utilization and prevent mode collapse in the mixture-of-experts, we incorporate an auxiliary load-balancing loss \mathcal{L}_{aux} , as formulated below:

$$\mathcal{L}_{\text{aux}} = \sum_{k=1}^K P_k \cdot f_k, \quad (29)$$

where P_k is the average routing probability for expert k , f_k is the fraction of samples assigned to that expert. The total training loss is then given by:

$$\mathcal{L}_{\text{ps}} = \mathcal{L}_{\text{ref}} + \gamma \mathcal{L}_{\text{aux}}, \quad (30)$$

where γ is a balanced weight that controls the trade-off between fusion quality and expert utilization.

IV. EXPERIMENTAL RESULTS AND ANALYSIS

In this section, we conduct comprehensive experiments to evaluate the performance of FoundPS. We first describe the experimental settings and implementation details. We then compare our approach with state-of-the-art methods on the proposed PSBench benchmark. Subsequently, ablation studies and efficiency analyses are performed to assess the effectiveness of individual design components. Finally, we evaluate the generalization capability, segmentation performance, and classical remote sensing applications of all methods.

A. Experiment Configurations

Extensive experiments are conducted on both reduced and full scales over PSBench. As for validation on the reduced scale, the degraded MS and PAN images are regarded as the inputs, and the original MS images are used as the groundtruth by following the Wald protocol [65]. We use four reference metrics, namely PSNR [85], SSIM [86], ERGAS [87] and SAM [88] to evaluate the fusion performance. It is worth mentioning that the larger values of PSNR and SSIM indicate the higher quality, while the smaller values of ERGAS and SAM



Fig. 8: 8-band visual comparisons of reduced scale on PSBench.

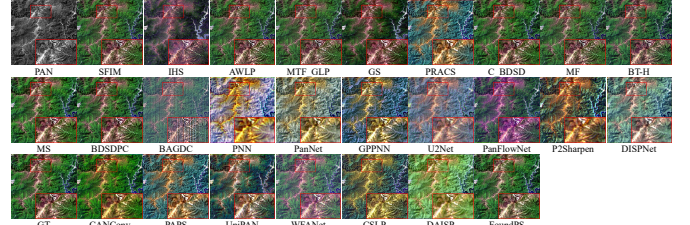


Fig. 9: 10-band visual comparisons of reduced scale on PSBench.

mean the better performance. As for the validation on the full scale, three mainstream metrics are used to assess the fusion performance, including D_λ , D_s , and QNR [89]. Notably, these non-reference metrics are evaluated on artificially manipulated parameters, which do not necessarily coincide with the visual effects. Several representative methods are selected for comprehensive comparisons at both reduced and full scales. Traditional methods include SFIM [73], IHS [42], AWLP [45], MTF_GLP [74], GS [44], PRACS [75], C_BDS [76], MF [77], BT-H [43], BDSDP [8] and BAGDC [50]. Deep learning methods are PNN [51], PanNet [52], GPPNN [78], U2Net [79], PanFlowNet [80], P2Sharpen [15], DISPNet [81], CANConv [82], PAPS [83], UniPAN [26], WFANet [84], CSLP [58] and DAISP [5]. For fairness, all deep learning methods are re-trained separately on task-specific datasets with necessary network modifications.

Our FoundPS is trained using 8 Nvidia A100 80GB GPUs with the PyTorch framework for 144h. Adam optimizer and L1 loss are employed for 500k iterations with a learning rate of $1e-4$. We set the batch size as 32 and distribute it evenly to each task. We randomly crop 256×256 PAN patches and MS patches with corresponding scale factor as network input for training and use 3 timesteps for both reduced- and full-scale testing. We modify the Infinite-UNet architecture by changing the channel number of the hidden layers D to obtain different versions with varied parameter quantities:

- FoundPS-T: $D=32$, channel multiplier = $\{1,1,1,1\}$
- FoundPS-S: $D=64$, channel multiplier = $\{1,1,1,1\}$
- FoundPS-B: $D=32$, channel multiplier = $\{1,2,2,4\}$
- FoundPS-L: $D=64$, channel multiplier = $\{1,2,2,4\}$

We adopt the default noise schedule and stationary variance $\lambda = 0.001$ in [68] with total diffusion steps as 1000. The hyper-parameters γ are set as 0.001.

B. Comparative Experiments

1) *Reduced-scale Assessment*: The qualitative results of reduced scale across different tasks are provided in Fig. 6,

TABLE II: Quantitative comparisons on reduced scale over the PSBench. The best and second best results are shown in **bold** and underline respectively. The up or down arrows indicate higher or lower values correspond to better results.

Method	Year	4 Bands				7 Bands				8 Bands				10 Bands				Average			
		PSNR↑	SSIM↑	ERGAS↓	SAM↓																
Traditional Method																					
SFIM [73]	2000	26.901	0.796	19.712	5.697	29.643	0.899	8.327	2.227	26.770	0.793	35.380	6.176	33.330	0.958	4.220	2.756	29.475	0.867	14.917	4.186
IHS [42]	2001	22.947	0.712	10.916	7.715	24.400	0.857	4.166	3.026	25.835	0.708	11.245	8.607	33.422	0.955	3.199	2.450	27.060	0.817	7.234	5.286
AWLP [45]	2005	28.919	0.799	6.916	6.998	28.923	0.744	2.586	2.160	24.520	0.782	10.888	10.929	34.180	0.867	2.509	1.960	29.994	0.809	5.286	5.065
MTF_GLP [74]	2006	24.682	0.771	16.405	6.401	20.445	0.866	4.878	1.842	26.609	0.772	10.462	6.104	32.696	0.955	3.091	1.237	26.833	0.848	9.115	3.854
GS [44]	2007	27.064	0.804	11.141	5.314	23.299	0.880	5.202	2.363	26.123	0.810	13.529	6.333	36.638	0.967	2.037	1.503	29.387	0.872	7.453	3.690
PRACS [75]	2010	28.298	0.762	8.300	7.238	27.835	0.708	3.505	3.684	26.815	0.760	10.846	8.887	31.732	0.794	4.545	3.801	29.121	0.763	6.590	5.722
C_BDSB [76]	2014	30.169	0.803	10.550	5.900	27.683	0.741	3.778	4.106	25.052	0.753	20.561	9.290	33.132	0.863	3.553	3.768	29.942	0.804	8.526	5.381
MF [77]	2016	24.726	0.773	25.941	5.498	25.574	0.899	10.479	3.032	27.600	0.818	30.155	5.544	33.300	0.959	4.229	2.694	28.107	0.863	16.696	4.147
BT-H [43]	2017	26.504	0.757	17.324	6.414	24.610	0.908	3.866	3.271	27.431	0.834	10.455	5.360	29.320	0.936	3.456	2.350	27.224	0.854	9.372	4.368
BDSBPC [8]	2019	30.107	0.751	9.054	6.005	29.891	0.781	2.857	2.955	24.062	0.637	14.902	9.459	34.333	0.874	3.192	2.863	30.561	0.780	6.891	4.941
BAGDC [50]	2021	28.507	0.737	9.180	4.965	29.581	0.707	2.229	1.331	22.292	0.614	17.573	9.017	33.396	0.803	2.492	1.721	29.384	0.735	6.987	3.852
Deep Learning Method																					
PNN [51]	2016	30.537	0.847	6.178	6.935	30.392	0.872	2.827	3.642	27.949	0.741	10.781	9.254	37.402	0.945	2.543	3.205	32.377	0.868	5.068	5.468
PanNet [52]	2017	30.649	0.857	7.330	8.023	31.484	0.903	2.491	3.328	28.796	0.799	13.157	10.502	38.524	0.959	1.749	2.847	33.103	0.890	5.498	5.856
GPPNN [78]	2021	31.553	0.856	6.481	6.561	32.063	0.921	2.296	2.987	29.696	0.815	10.490	8.893	39.871	0.966	1.681	2.464	34.093	0.898	4.754	4.926
U2Net [79]	2023	32.078	0.826	6.128	4.946	31.378	0.815	2.496	2.513	30.060	0.785	9.269	5.176	39.136	0.935	1.698	2.511	33.966	0.854	4.493	3.749
PanFlowNet [80]	2023	32.938	0.887	5.711	5.918	32.699	0.917	1.988	2.638	30.504	0.836	9.864	8.953	40.361	0.979	1.757	1.505	34.966	0.915	4.364	4.335
P2Sharpen [81]	2023	32.249	0.893	11.359	5.379	34.876	0.936	1.533	2.068	30.631	0.848	9.461	7.236	40.181	0.958	1.558	2.263	35.076	0.915	6.118	4.042
DISPNet [15]	2024	32.732	0.892	8.139	4.837	35.443	0.939	1.408	1.738	31.910	0.877	7.244	5.438	40.538	0.976	1.327	2.107	35.650	0.926	4.577	3.479
CANConv [82]	2024	33.129	0.873	6.185	4.652	35.111	0.932	1.964	2.040	32.302	0.879	7.399	5.578	40.139	0.982	1.510	2.366	35.655	0.920	4.081	3.574
PAPS [83]	2024	33.053	0.883	5.619	5.429	35.242	0.944	1.489	1.849	32.958	0.903	7.343	5.102	41.078	0.969	1.333	1.968	36.056	0.925	3.733	3.609
UniPAN [26]	2025	33.836	0.892	6.007	4.970	35.587	0.945	1.535	1.947	30.323	0.827	9.449	8.065	41.879	0.979	1.299	1.923	36.263	0.920	4.175	3.889
WFANet [84]	2025	32.693	0.868	5.722	5.842	37.098	0.928	1.314	1.513	33.283	0.895	6.063	5.383	43.365	0.967	1.109	1.492	37.059	0.915	3.476	3.578
CSLP [58]	2025	35.506	0.906	4.346	3.306	36.873	0.948	1.319	1.630	33.156	0.902	6.859	4.887	41.380	0.979	1.375	1.824	37.326	0.937	3.204	2.755
DAISP [5]	2025	34.577	0.897	5.653	4.326	37.087	0.950	1.251	1.589	32.608	0.892	7.016	4.967	42.474	0.977	1.144	1.647	37.320	0.932	3.592	3.055
Universal Method																					
FoundPS-T	-	35.945	0.919	3.893	3.396	39.444	0.960	0.995	1.114	32.853	0.891	6.156	5.473	44.525	0.987	1.047	1.372	38.922	0.945	2.775	2.630
FoundPS-S	-	37.153	0.931	3.831	2.768	39.614	0.961	0.973	1.091	33.803	0.915	6.896	4.568	45.892	0.987	0.772	1.134	39.958	0.952	2.769	2.197
FoundPS-B	-	37.460	0.934	3.590	2.682	40.903	0.969	0.856	0.954	33.961	0.916	5.729	4.410	46.298	0.989	0.836	1.104	40.451	0.955	2.513	2.110
FoundPS-L	-	37.825	0.937	3.522	2.572	41.420	0.973	0.801	0.924	34.280	0.921	5.517	4.659	47.596	0.991	0.660	0.944	41.141	0.959	2.391	2.050

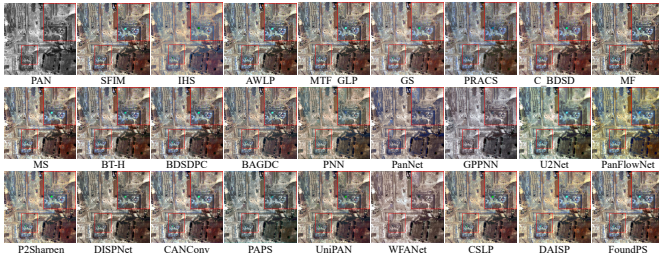


Fig. 10: 4-band visual comparisons of full scale on PSBench.

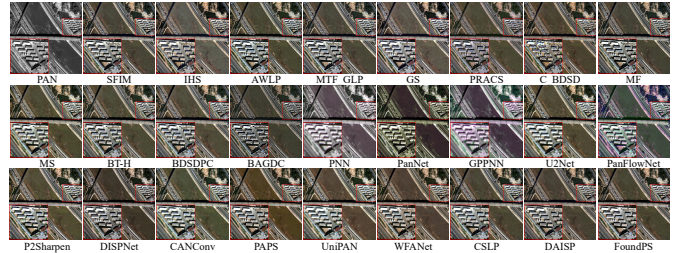


Fig. 12: 8-band visual comparisons of full scale on PSBench.

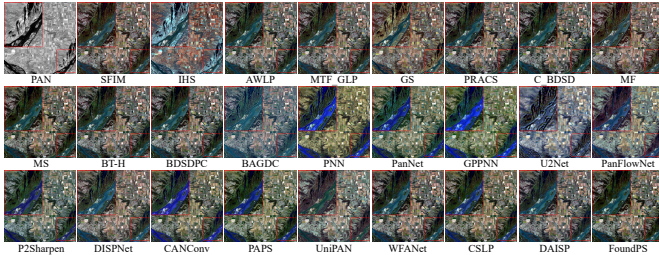


Fig. 11: 7-band visual comparisons of full scale on PSBench.

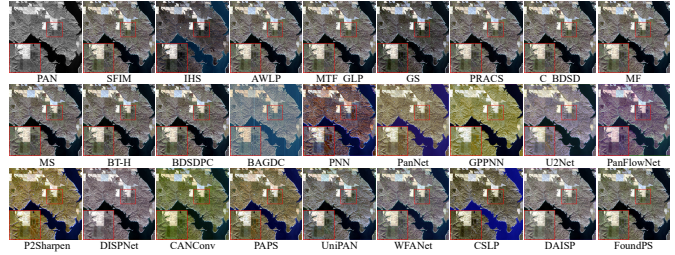


Fig. 13: 10-band visual comparisons of full scale on PSBench.

Fig. 7, Fig. 8, and Fig. 9, respectively. Apparently, traditional methods show spectral distortions due to the unbalanced combination of PAN-derived spatial cues. Deep methods improve on the integration of spectral and spatial information, yet our proposed method stands out with a more accurate spectral distribution and enhanced spatial detail. To statistically validate the performance, we report the quantitative results in Tab. II. For fairness, we deactivate BPS. Our method achieves the best average value in all metrics, indicating that the fused results

are the most similar to the reference. Therefore, our method outperforms other methods and is the most competitive.

2) *Full-scale Assessment*: We also measure the fusion performance on full scale. The visual comparisons are shown in Fig. 10, Fig. 11, Fig. 12, and Fig. 13. Regarding the traditional methods, some of them appropriately retain similar spectral attributes with the MS image but inadequately integrate the spatial details, while others distort both spectral and spatial information. As for deep methods, some of them struggle

TABLE III: Quantitative comparisons on full scale over the PSBench. The best and second best results are shown in **bold** and underline respectively. The up or down arrows indicate higher or lower values correspond to better results.

Method	Year	4 Bands			7 Bands			8 Bands			10 Bands			Average		
		QNR↑	D_λ ↓	D_s ↓												
Traditional Method																
SFIM [73]	2000	0.7849	0.0919	0.1372	0.8115	0.0768	0.1227	0.8437	0.0719	0.0918	0.8158	0.0580	0.1343	0.8084	0.0752	0.1270
IHS [42]	2001	0.5925	0.1055	0.3393	0.6957	0.1360	0.2002	0.8112	0.0875	0.1128	0.7444	0.1408	0.1356	0.6928	0.1198	0.2145
AWLP [45]	2005	0.7733	0.0839	0.1619	0.8032	0.0984	0.1112	0.8533	0.0486	0.1042	0.7354	0.1550	0.1305	0.7780	0.1046	0.1341
MTF_GLP [74]	2006	0.7054	0.1175	0.2051	0.8200	0.0880	0.1035	0.8064	0.0855	0.1196	0.7725	0.0520	0.1857	0.7627	0.0861	0.1680
GS [44]	2007	0.6515	0.0681	0.3064	0.7734	0.0787	0.1654	0.8625	0.0426	0.0998	0.8235	0.0507	0.1335	0.7606	0.0605	0.1942
PRACS [75]	2010	0.6979	0.0921	0.2436	0.7238	0.1479	0.1537	0.7620	0.1172	0.1382	0.7486	0.1130	0.1571	0.7286	0.1126	0.1837
C_BSDS [76]	2014	0.9173	0.0307	0.0544	0.8075	0.0899	0.1137	0.8020	0.0595	0.1472	0.8252	0.0516	0.1306	0.8506	0.0523	0.1036
MF [77]	2016	0.7162	0.1135	0.1964	0.7570	0.0996	0.1610	0.8346	0.0768	0.0971	0.7911	0.0719	0.1480	0.7654	0.0920	0.1596
BT-H [43]	2017	0.6991	0.1360	0.2056	0.8299	0.0792	0.1002	0.8545	0.0546	0.0979	0.7533	0.0904	0.1724	0.7631	0.0990	0.1601
BSDSPC [8]	2019	0.9038	0.0347	0.0657	0.8190	0.0817	0.1093	0.8590	0.0498	0.0973	0.7517	0.0981	0.1677	0.8323	0.0661	0.1115
BAGDC [50]	2021	0.8306	0.0826	0.1040	0.6927	0.2217	0.1117	0.7539	0.1090	0.1541	0.6311	0.2238	0.1874	0.7294	0.1575	0.1400
Deep Learning Method																
PNN [51]	2016	0.6454	0.1459	0.2484	0.7985	0.1125	0.1013	0.7992	0.0889	0.1230	0.7035	0.1307	0.1922	0.7144	0.1266	0.1853
PanNet [52]	2017	0.6151	0.1285	0.2971	0.8157	0.0816	0.1124	0.8162	0.0818	0.1116	0.7322	0.1274	0.1619	0.7188	0.1129	0.1926
GPPNN [78]	2021	0.6313	0.1474	0.2638	0.7673	0.1011	0.1471	0.7969	0.1039	0.1118	0.7681	0.1139	0.1337	0.7247	0.1218	0.1780
U2Net [79]	2023	0.8469	0.0696	0.0897	0.7984	0.1107	0.1028	0.8639	0.0272	0.1121	0.7167	0.1366	0.1706	0.7981	0.0926	0.1218
PanFlowNet [80]	2023	0.7472	0.1273	0.1459	0.7731	0.1073	0.1347	0.8254	0.0792	0.1038	0.8160	0.0698	0.1230	0.7859	0.0978	0.1302
P2Sharpen [15]	2023	0.7819	0.0520	0.1758	0.8054	0.0728	0.1321	0.8554	0.0595	0.0908	0.7937	0.0886	0.1293	0.8008	0.0688	0.1403
DISPNet [81]	2024	0.7682	0.0903	0.1560	0.8413	0.0553	0.1097	0.8274	0.0918	0.0895	0.8133	0.0612	0.1341	0.8047	0.0748	0.1308
CANConv [82]	2024	0.7768	0.0416	0.1915	0.8208	0.0642	0.1233	0.8631	0.0513	0.0907	0.8280	0.0532	0.1257	0.8141	0.0509	0.1430
PAPS [83]	2024	0.7439	0.1164	0.1597	0.8065	0.0782	0.1260	0.8503	0.0593	0.0965	0.7917	0.0964	0.1242	0.7864	0.0946	0.1328
UniPAN [26]	2025	0.7780	0.0693	0.1640	0.8121	0.0696	0.1278	0.8601	0.0557	0.0893	0.8286	0.0609	0.1178	0.8127	0.0646	0.1314
WFANet [84]	2025	0.7109	0.1030	0.2062	0.8512	0.0453	0.1086	0.8560	0.0619	0.0878	0.7969	0.0789	0.1351	0.7854	0.0788	0.1481
CSLP [58]	2025	0.7782	0.0707	0.1641	0.8300	0.0556	0.1216	0.8618	0.0530	0.0908	0.8226	0.0651	0.1202	0.8143	0.0636	0.1314
DAISP [5]	2025	0.7805	0.0619	0.1688	0.8342	0.0481	0.1242	0.8152	0.0911	0.1041	0.8211	0.0515	0.1346	0.8085	0.0603	0.1401
Universal Method																
FoundPS-T	-	0.9189	0.0301	0.0531	0.8641	0.0314	0.1081	0.8738	0.0517	0.0788	0.8585	0.0345	0.1109	0.8827	0.0349	0.0856
FoundPS-S	-	0.8985	0.0303	0.0740	0.8625	0.0304	0.1106	0.8853	0.0346	0.0834	0.8479	0.0425	0.1147	0.8736	0.0349	0.0952
FoundPS-B	-	0.9266	0.0202	0.0546	0.8860	0.0185	0.0973	0.9008	0.0249	0.0763	0.8458	0.0372	0.1217	0.8891	0.0262	0.0874
FoundPS-L	-	0.9291	0.0206	0.0517	0.8938	0.0142	0.0933	0.8979	0.0298	0.0746	0.8687	0.0222	0.1116	0.8985	0.0213	0.0821

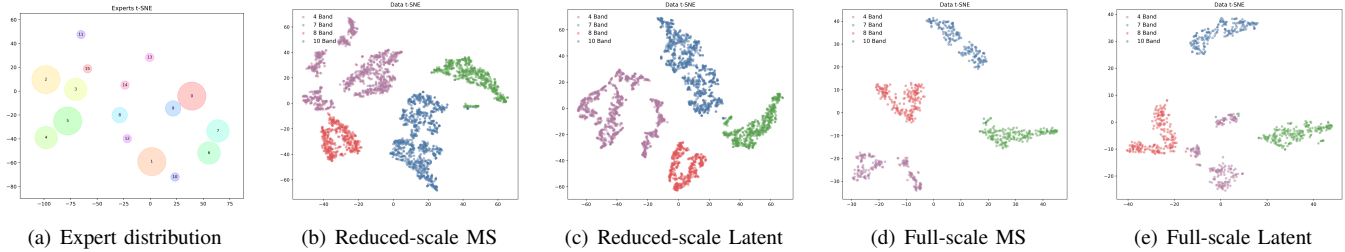


Fig. 14: Distribution of data and parameters by t-SNE visualization. (a) Expert parameters and their activation frequency. Larger circles represent higher activation frequencies. (b) MS images on the reduced scale. (c) MS latents generated by MiT on the reduced scale. (d) MS images on the full scale. (e) MS latents generated by MiT on the full scale.

to maintain the balance between the preservation of spectral distribution and the injection of spatial details, while others reasonably inject the spatial details and enhance the fusion quality. The quantitative results are presented in Tab. III. Our method still secures the top spot on non-reference metrics and thus maintains a leading edge.

C. Ablation Study

To fully exploit the effectiveness of each design, we conduct ablation studies that include three categories: (i) Distributions and effects of the experts in MiT, (ii) diffusion sampling steps and strategies, and (iii) scalability of the FoundPS variants.

1) *Distributions and Effects of Experts in MiT*: To thoroughly evaluate the role of the mixture-of-experts, we first present the distributions of expert parameters and activation

frequencies on PSBench, as illustrated in Fig. 14(a). Obviously, experts exhibit consistent assignment preferences to specific spectral bands, with larger circles indicating higher activation frequencies. This pattern confirms that MiT effectively learns band-wise modal specialization through dynamic expert routing. Furthermore, we visualize the distributions of MS-pixel and MS-latent features on PSBench at both reduced and full scales, as shown in Fig. 14. The results show that MiT consistently preserves the independence of distributions for data from different satellite sensors or scenes. Therefore, FoundPS is able to process data with heterogeneous distribution characteristics in a unified and coherent manner.

2) *Diffusion Sampling Steps and Strategies*: Model efficiency and fusion quality depend on the sampling steps, quantified by neural function evaluations (NFEs). We provide the fusion performance of different sampling steps in Tab. IV

TABLE IV: Pansharpener performance of reduced scale with different sampling steps.

NFEs	4 Bands				7 Bands				8 Bands				10 Bands				Average			
	PSNR \uparrow	SSIM \uparrow	ERGAS \downarrow	SAM \downarrow	PSNR \uparrow	SSIM \uparrow	ERGAS \downarrow	SAM \downarrow	PSNR \uparrow	SSIM \uparrow	ERGAS \downarrow	SAM \downarrow	PSNR \uparrow	SSIM \uparrow	ERGAS \downarrow	SAM \downarrow	PSNR \uparrow	SSIM \uparrow	ERGAS \downarrow	SAM \downarrow
1	33.232	0.843	6.218	3.220	37.949	0.945	1.144	1.195	28.610	0.765	11.337	4.879	45.126	0.980	0.849	0.972	37.285	0.895	4.304	2.366
3	37.824	0.937	3.522	2.571	41.420	0.973	0.801	0.924	34.281	0.921	5.517	4.659	47.596	0.992	0.660	0.944	41.142	0.959	2.391	2.050
5	37.618	0.934	3.616	2.626	40.985	0.970	0.839	0.957	33.989	0.917	5.674	4.732	47.240	0.991	0.685	0.970	40.833	0.956	2.462	2.094
10	37.425	0.932	3.735	2.694	40.808	0.970	0.852	0.973	33.523	0.911	5.935	4.872	47.021	0.990	0.704	0.990	40.594	0.955	2.549	2.148

TABLE V: Pansharpener performance of full scale with different sampling steps.

NFEs	4 Bands			7 Bands			8 Bands			10 Bands			Average		
	QNR \uparrow	D_λ \downarrow	D_s \downarrow	QNR \uparrow	D_λ \downarrow	D_s \downarrow	QNR \uparrow	D_λ \downarrow	D_s \downarrow	QNR \uparrow	D_λ \downarrow	D_s \downarrow	QNR \uparrow	D_λ \downarrow	D_s \downarrow
1	0.9240	0.0050	0.0714	0.9262	0.0119	0.0627	0.8906	0.0048	0.1052	0.9042	0.0016	0.0944	0.9130	0.0051	0.0823
3	0.9291	0.0206	0.0517	0.8938	0.0142	0.0933	0.8979	0.0298	0.0746	0.8687	0.0222	0.1116	0.8985	0.0213	0.0821
5	0.9385	0.0124	0.0499	0.9066	0.0086	0.0856	0.9111	0.0174	0.0728	0.8789	0.0153	0.1075	0.9093	0.0134	0.0785
10	0.9309	0.0195	0.0510	0.8955	0.0132	0.0926	0.9031	0.0240	0.0748	0.8705	0.0206	0.1112	0.9007	0.0194	0.0816

TABLE VI: Reduced-scale fusion performance of different η via bridge posterior sampling (FoundPS-L).

η	4 Bands				7 Bands				8 Bands				10 Bands				Average			
	PSNR \uparrow	SSIM \uparrow	ERGAS \downarrow	SAM \downarrow	PSNR \uparrow	SSIM \uparrow	ERGAS \downarrow	SAM \downarrow	PSNR \uparrow	SSIM \uparrow	ERGAS \downarrow	SAM \downarrow	PSNR \uparrow	SSIM \uparrow	ERGAS \downarrow	SAM \downarrow	PSNR \uparrow	SSIM \uparrow	ERGAS \downarrow	SAM \downarrow
0	37.8246	0.9370	3.5224	2.5717	41.4200	0.9731	0.8010	0.9240	34.2805	0.9208	5.5171	4.6592	47.5956	0.9915	0.6600	0.9438	41.1415	0.9589	2.3913	2.0504
0.01	37.8249	0.9370	3.5224	2.5717	41.4201	0.9731	0.8010	0.9240	34.2798	0.9208	5.5173	4.6593	47.5957	0.9915	0.6600	0.9438	41.1415	0.9589	2.3913	2.0504
0.02	37.8252	0.9370	3.5223	2.5716	41.4202	0.9731	0.8009	0.9240	34.2790	0.9208	5.5175	4.6594	47.5957	0.9915	0.6600	0.9438	41.1416	0.9589	2.3913	2.0504
0.05	37.8262	0.9370	3.5221	2.5715	41.4206	0.9731	0.8009	0.9240	34.2767	0.9208	5.5181	4.6597	47.5958	0.9915	0.6600	0.9438	41.1417	0.9589	2.3913	2.0504
0.1	37.8276	0.9371	3.5218	2.5712	41.4213	0.9731	0.8008	0.9240	34.2725	0.9208	5.5192	4.6602	47.5960	0.9915	0.6600	0.9438	41.1417	0.9589	2.3914	2.0504
0.5	37.8269	0.9370	3.5231	2.5708	41.4263	0.9731	0.8004	0.9237	34.2252	0.9205	5.5331	4.6660	47.5975	0.9915	0.6598	0.9438	41.1359	0.9589	2.3937	2.0510
1.0	37.8043	0.9369	3.5311	2.5735	41.4318	0.9731	0.7999	0.9235	34.1369	0.9198	5.5603	4.6769	47.5992	0.9915	0.6597	0.9437	41.1167	0.9587	2.4004	2.0535
5.0	37.2621	0.9320	3.7161	2.6591	41.4542	0.9732	0.7980	0.9228	32.9470	0.9091	5.9754	4.8453	47.6059	0.9915	0.6593	0.9435	40.7601	0.9555	2.5250	2.1077
10.0	36.3661	0.9227	4.0468	2.8302	41.4467	0.9732	0.7987	0.9239	31.4684	0.8912	6.6353	5.1364	47.6027	0.9915	0.6595	0.9439	40.2299	0.9496	2.7368	2.2101

TABLE VII: Full-scale fusion performance of different η via bridge posterior sampling (FoundPS-L).

η	4 Bands			7 Bands			8 Bands			10 Bands			Average		
	QNR \uparrow	D_λ \downarrow	D_s \downarrow	QNR \uparrow	D_λ \downarrow	D_s \downarrow	QNR \uparrow	D_λ \downarrow	D_s \downarrow	QNR \uparrow	D_λ \downarrow	D_s \downarrow	QNR \uparrow	D_λ \downarrow	D_s \downarrow
0	0.9220	0.0234	0.0564	0.8915	0.0149	0.0950	0.8941	0.0302	0.0782	0.8666	0.0237	0.1125	0.8943	0.0230	0.0849
0.01	0.9220	0.0234	0.0564	0.8915	0.0149	0.0950	0.8941	0.0302	0.0782	0.8666	0.0237	0.1125	0.8943	0.0230	0.0849
0.02	0.9219	0.0234	0.0564	0.8915	0.0149	0.0950	0.8941	0.0302	0.0782	0.8666	0.0237	0.1125	0.8943	0.0230	0.0849
0.05	0.9219	0.0234	0.0564	0.8915	0.0149	0.0950	0.8941	0.0302	0.0782	0.8666	0.0237	0.1125	0.8943	0.0230	0.0849
0.1	0.9219	0.0234	0.0564	0.8915	0.0149	0.0950	0.8941	0.0302	0.0782	0.8666	0.0237	0.1125	0.8943	0.0230	0.0849
0.5	0.9218	0.0235	0.0564	0.8914	0.0150	0.0951	0.8942	0.0302	0.0781	0.8666	0.0237	0.1125	0.8942	0.0230	0.0849
1.0	0.9217	0.0235	0.0565	0.8913	0.0151	0.0951	0.8944	0.0299	0.0782	0.8666	0.0237	0.1124	0.8942	0.0230	0.0849
5.0	0.9214	0.0234	0.0569	0.8905	0.0157	0.0954	0.8952	0.0282	0.0789	0.8667	0.0237	0.1123	0.8941	0.0228	0.0852
10.0	0.9201	0.0239	0.0578	0.8896	0.0165	0.0955	0.8916	0.0307	0.0802	0.8669	0.0236	0.1122	0.8931	0.0235	0.0856

and Tab. V for reduced and full scale, respectively. In $\widehat{\mathbf{z}}_0^t$ -prediction mode, FoundPS-L shows a clear trend in reduced-scale testing. Initially, performance improves with more steps, peaking at 3 NFEs due to the accuracy gain from additional refinement. Beyond this point, further increases in NFEs lead to a gradual performance decline, likely caused by iterative over-refinement that perturbs the converged optimal solution. In full-scale testing, FoundPS-L yields the best result, followed by a drop at 3 NFEs and a secondary peak at 5 NFEs. Considering performance and efficiency across both evaluation regimes, we set 3 sampling steps as the operational default.

Furthermore, we evaluate the latent bridge posterior sampling strategies with different weights η . The quantitative comparisons are reported in Tab. VI and Tab. VII for reduced- and full-scale testing, respectively. Notably, we crop the image pairs for full-scale evaluation due to overloading GPU memory. The results reveal that small values of η yield stable and near-optimal performance across all spectral configurations at both two scales. At reduced scale, PSNR and SSIM peak around $\eta = 0.1$ and gradually decline as η increases beyond 0.5, indicating that excessive posterior guidance can over-constrain the diffusion process and degrade fusion qual-

ity. In contrast, full-scale metrics remain largely stable for $\eta \leq 1.0$, demonstrating the robustness of the sampling strategy to moderate guidance strengths. Notably, $\eta = 0$ already achieves competitive results, suggesting that our latent diffusion bridge is well optimized and can provide strong latent regularization. Based on these observations, BPS is capable of serving as a training-free fusion adaptation mechanism, offering controllable guidance for pansharpener task.

3) *Scalability of the FoundPS variants*: To demonstrate our scalability, we construct multiple FoundPS variants by adjusting the feature channels in Infinite-UNet, thereby varying model capacity. Quantitative results on both reduced and full scales are summarized in Tab. II and Tab. III, respectively. The results clearly indicate that performance scales positively with parameter count, confirming the architecture’s ability to leverage increased capacity. Notably, even the tiny variant FoundPS-T remains competitive against task-specific methods, underscoring the effectiveness of the proposed method.

D. Efficiency Analysis

We conduct the efficiency analysis experiments to record model parameters, floating point operations (FLOPs), GPU

TABLE VIII: Model efficiency and details of deep pansharpening methods.

Method	PNN [51]	PanNet [52]	GPPNN [78]	U2Net [79]	PanFlowNet [80]	P2Sharpen [15]	DISPNet [81]	CANConv [82]	PAPS [83]	UniPAN [26]	WFANet [84]	CSLP [58]	DAISP [5]	FoundPS-T	FoundPS-S	FoundPS-B	FoundPS-L
Parameters (M)	0.081	0.095	0.119	0.527	0.087	0.715	1.566	0.199	1.141	0.076	0.506	1.209	2.324	5.249	8.965	8.315	20.661
FLOPs (G)	5.263	6.221	5.586	8.301	22.850	46.547	110.667	1.614	80.971	4.982	12.323	27.621	135.640	36.798	105.383	47.057	144.429
GPU Memory (G)	0.593	0.546	0.667	0.702	0.606	1.093	0.589	0.979	0.757	0.548	0.831	0.655	0.899	1.032	1.177	1.055	1.255
Time (s)	0.061	0.082	0.093	0.164	0.130	0.173	0.179	0.217	0.167	0.076	0.166	0.130	0.183	0.346	0.471	0.748	0.945

TABLE IX: Pansharpening performance generalize on unseen scene datasets (SegGF). **Bold** means the best fusion performance.

Method	PSNR \uparrow	SSIM \uparrow	ERGAS \downarrow	SAM \downarrow	QNR \uparrow	D_λ \downarrow	D_s \downarrow
SFIM [73]	23.5614	0.6119	4.4906	2.8847	0.7420	0.0970	0.1795
IHS [42]	25.0828	0.6447	3.6904	2.5954	0.5248	0.1513	0.3835
AWLP [45]	23.7044	0.5657	4.1370	2.2204	0.6564	0.1413	0.2368
MTF_GLP [74]	22.8603	0.5300	4.7263	3.0044	0.6224	0.1662	0.2547
GS [44]	25.5757	0.6511	3.4430	2.6016	0.5179	0.1490	0.3930
PRACS [75]	22.3317	0.5296	5.1180	3.6990	0.5437	0.2189	0.3080
C_BDSB [76]	23.3529	0.6025	4.4834	4.0230	0.8375	0.0284	0.1382
MF [77]	25.1288	0.6456	3.6448	2.4158	0.6274	0.1664	0.2483
BT-H [43]	23.9201	0.6108	4.3272	3.6216	0.6130	0.1442	0.2845
BDSBPC [8]	25.4260	0.6471	3.5567	2.9257	0.8171	0.0374	0.1515
BAGDC [50]	25.2113	0.5981	3.4773	<u>2.1423</u>	0.8237	0.1041	<u>0.0825</u>
PNN [51]	24.1732	0.6991	3.9805	5.0416	0.3723	0.3458	0.4330
PanNet [52]	20.8404	0.5865	6.1647	10.2467	0.5113	0.3108	0.2622
GPPNN [78]	24.0514	0.6990	4.2215	5.6822	0.6025	0.2178	0.2296
U2Net [79]	22.4246	0.7077	5.7532	6.6718	<u>0.8453</u>	0.0479	0.1127
PanFlowNet [80]	12.7717	0.4703	30.0502	14.0260	0.3733	0.3367	0.4331
P2Sharpen [15]	22.3037	0.7225	4.1746	3.5671	0.5131	0.1914	0.3669
DISPNet [81]	24.2749	0.7382	4.7943	3.9017	0.8366	0.0460	0.1233
CANConv [82]	27.0788	<u>0.8139</u>	3.1013	4.0545	0.8417	0.0453	0.1187
PAPS [83]	22.2894	0.7305	4.5931	8.8448	0.5202	0.2344	0.3208
UniPAN [26]	27.8065	0.7565	2.7156	2.4996	0.5909	0.1491	0.3079
WFANet [84]	18.9564	0.6613	5.7413	7.1638	0.6246	0.2006	0.2186
CSLP [58]	<u>28.9008</u>	0.7695	<u>2.2789</u>	2.5067	0.7327	0.0671	0.2163
DAISP [5]	19.7114	0.6866	9.0789	4.9151	0.6437	0.1703	0.2247
FoundPS-L	35.2662	0.9369	1.1393	1.3139	0.9002	0.0373	0.0650

TABLE X: Pansharpening performance generalize on unseen Quickbird satellite datasets. **Bold** means the best performance.

Method	PSNR \uparrow	SSIM \uparrow	ERGAS \downarrow	SAM \downarrow	QNR \uparrow	D_λ \downarrow	D_s \downarrow
SFIM [73]	32.1191	0.8428	3.2205	2.8913	0.7491	0.1130	0.1619
IHS [42]	33.9318	0.8593	2.6920	2.9892	0.6243	0.1566	0.2676
AWLP [45]	31.0584	0.8318	3.2075	2.7981	0.7580	0.1026	0.1581
MTF_GLP [74]	31.4792	0.8169	3.3763	2.9041	0.7064	0.1380	0.1854
GS [44]	34.4601	0.8785	2.4205	2.6338	0.7098	0.0989	0.2165
PRACS [75]	31.9727	0.8344	3.1957	3.2070	0.7512	0.1164	0.1556
C_BDSB [76]	31.2896	0.8483	3.5112	3.7471	<u>0.9027</u>	<u>0.0318</u>	<u>0.0692</u>
MF [77]	31.7826	0.8475	3.3396	<u>2.7088</u>	0.7061	0.1346	0.1879
BT-H [43]	33.3582	0.8668	2.6727	2.6542	0.7502	0.1056	0.1668
BDSBPC [8]	<u>34.3902</u>	<u>0.8847</u>	<u>2.3898</u>	2.7977	0.8034	0.0662	0.1443
BAGDC [50]	31.9780	0.8378	3.2547	3.0739	0.7238	0.1799	0.1217
PNN [51]	24.9903	0.8396	7.5687	11.6871	0.4390	0.3531	0.3240
PanNet [52]	21.6332	0.7963	12.6515	14.6404	0.4285	0.3783	0.3154
GPPNN [78]	26.3027	0.8616	6.9445	11.7491	0.7272	0.1443	0.1529
U2Net [79]	27.4097	0.7240	5.5303	8.7204	0.7961	0.1087	0.1081
PanFlowNet [80]	21.4585	0.7554	17.6751	13.2153	0.6191	0.1689	0.2560
P2Sharpen [15]	33.3422	0.8840	2.8564	3.3286	0.6301	0.1638	0.2509
DISPNet [81]	31.0746	0.8446	3.4811	4.6411	0.8618	0.0633	0.0856
CANConv [82]	33.5858	<u>0.8930</u>	2.9639	3.1327	0.8863	0.0350	0.0816
PAPS [83]	29.9086	0.8828	4.0986	7.8094	0.7588	0.1240	0.1343
UniPAN [26]	29.5113	0.8885	4.8035	3.2952	0.6353	0.1412	0.2635
WFANet [84]	26.2470	0.8453	6.7174	10.7235	0.6647	0.1907	0.1809
CSLP [58]	31.2616	0.8801	4.3995	3.7732	0.7919	0.1204	0.0982
DAISP [5]	25.7630	0.8054	9.0269	5.0775	0.6924	0.1353	0.2039
FoundPS-L	38.9823	0.9545	1.4540	1.7429	0.9224	0.0224	0.0566

memory usage, and time consumption of the deep-learning-based pansharpening method on 4-band data of PSBench with PAN size of 256×256 and MS size of $64 \times 64 \times 4$. The results are detailed in Tab. VIII. Clearly, most deep learning methods exhibit high processing speeds for test image samples. However, practical deployment requires training and maintaining separate models for individual satellite sensors, severely limits their scalability. In comparison, our FoundPS introduces additional computational overhead due to its band-agnostic representation learning and diffusion-based fusion framework.

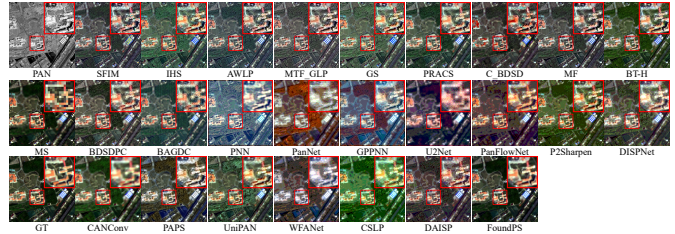


Fig. 15: Visual comparisons of reduced scale on SegGF.

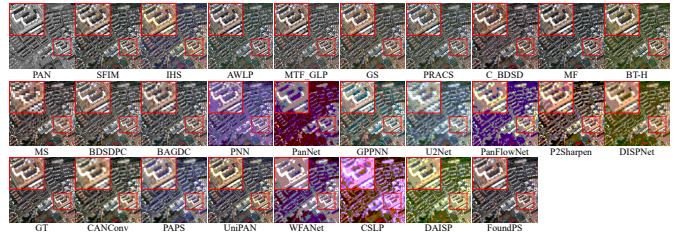


Fig. 16: Visual comparisons of reduced scale on Quickbird.

Notably, FoundPS-T and FoundPS-S deliver competitive fusion performance with computational costs comparable to or lower than many contemporary approaches, demonstrating that our architecture is able to effectively strike a balance between performance and practicality.

E. Generalize on Unseen Scene and Satellites

To verify the superiority of our universal pansharpening paradigm, we initially generalize all pretrained models from SegGF [5] for unseen scene generalization, which is captured by the GaoFen-2 satellite but excluded in PSBench. Results in Tab. IX show that FoundPS-L significantly outperforms all the task-specific methods. Moreover, we utilize all models to generalize on the datasets captured by the Quickbird satellite, as shown in Tab. X. Besides, the visualizations on both scale across these datasets are presented in Fig. 15, Fig. 16, Fig. 17, and Fig. 18. Evidently, our method retains substantial advantages over both traditional and deep-learning methods.

F. Application Verification on Segmentation

SegGF dataset is also specifically designed to overcome the limitations of no-reference evaluation metrics by providing meticulously crafted and highly reliable semantic labels. Therefore, we employ a unified multi-modal segmentation model SegFormer [91] to rigorously assess the pansharpening performance of each method. For comprehensive comparisons, the mono-channel PAN images, along with resized low-quality MS images, are considered to provide basic segmentation reference. The qualitative results on reduced scale and full scale are illustrated in Fig. 19 and Fig. 20, respectively. Although PAN images contain more spatial details, their

Method	Reduced-scale												Full-scale											
	Accuracy						IoU [90]						Accuracy						IoU [90]					
	Avg.	Land.	Build.	Road.	Vega.	Water.	Avg.	Land.	build.	Road.	Vega.	water.	Avg.	Land.	Build.	Road.	Vega.	Water.	Avg.	Land.	build.	Road.	Vega.	water.
PAN	46.29	37.17	60.37	36.82	67.57	75.82	31.38	31.31	38.72	25.75	42.35	50.18	50.09	50.08	67.24	58.20	58.32	66.72	35.48	38.58	45.80	35.49	41.89	51.12
LRMS	54.84	71.18	59.27	47.72	83.13	67.76	42.52	57.76	47.60	33.16	62.05	42.35	57.15	73.46	71.90	48.77	82.28	66.46	44.83	59.05	52.94	37.38	63.97	55.64
SFIM [73]	56.42	71.97	69.05	46.11	79.23	72.16	43.14	58.54	49.63	33.35	62.09	55.23	60.06	78.78	69.00	59.32	78.57	74.68	47.59	61.17	56.28	43.19	64.20	60.70
IHS [42]	56.05	72.16	67.40	42.84	79.40	74.51	42.49	57.64	49.87	31.62	61.31	54.49	57.40	76.09	74.79	54.30	80.62	58.63	45.53	59.45	55.92	40.68	64.61	52.52
AWLP [45]	56.09	72.00	64.75	48.09	80.56	71.15	43.10	58.33	48.73	34.07	62.48	55.01	56.76	74.10	64.26	52.52	86.36	63.31	45.47	56.51	54.10	40.32	65.88	55.99
MTF_GLP [74]	56.83	69.80	66.48	44.87	82.57	77.25	43.13	58.22	51.19	33.32	62.75	53.28	58.00	78.26	68.75	57.99	80.75	62.22	46.31	57.98	56.26	42.94	65.75	54.92
GS [44]	55.86	69.76	66.91	44.80	81.30	72.37	42.79	57.38	50.25	32.35	61.55	55.22	57.39	70.84	71.09	54.24	80.48	67.72	44.93	59.44	52.72	37.91	63.05	56.43
PRACS [75]	57.00	71.37	67.50	45.48	80.59	77.04	43.19	58.38	51.42	33.53	62.33	53.51	56.72	74.57	68.87	51.20	84.70	60.98	45.14	57.18	55.52	39.51	65.41	53.19
C_BDS [76]	55.44	70.27	67.59	46.15	81.52	67.11	42.81	57.89	49.32	32.83	62.43	54.38	57.97	79.09	69.17	55.16	81.47	62.96	46.43	57.70	56.83	42.14	65.97	55.92
MF [77]	55.57	72.01	61.72	49.62	81.20	68.87	42.96	58.17	47.97	34.18	62.46	54.95	56.72	77.96	71.29	58.54	79.26	53.30	44.92	57.86	56.24	42.63	64.76	48.04
BT-H [43]	54.75	71.11	68.79	44.04	82.18	62.41	42.45	57.84	49.77	32.02	62.46	52.58	57.83	73.06	75.23	46.04	81.82	70.81	44.81	59.84	52.73	36.07	64.73	55.51
BDS [8]	55.84	71.44	69.64	46.20	80.82	66.97	43.22	58.54	50.59	33.18	62.34	54.69	58.55	79.76	63.78	59.17	79.86	68.75	46.75	59.39	54.00	43.27	64.30	59.56
BAGDC [50]	55.46	70.22	62.47	45.94	84.13	69.99	42.77	57.76	49.65	33.35	62.50	53.35	57.38	74.30	65.59	51.36	85.61	67.44	45.87	57.05	54.72	39.68	65.47	58.29
PNN [51]	55.58	68.04	55.10	48.60	83.11	78.63	41.22	57.33	45.58	35.07	61.85	47.52	57.93	72.29	77.44	61.52	79.92	56.39	45.77	59.16	55.89	44.18	65.07	50.34
PanNet [52]	55.14	69.24	64.98	47.85	78.18	70.61	41.84	54.98	46.19	34.58	60.39	54.87	58.07	74.16	64.56	55.16	82.25	72.30	45.52	58.41	51.11	41.08	64.80	57.69
GPPNN [78]	56.51	69.63	71.06	46.31	79.82	72.24	43.42	57.56	50.67	34.64	60.78	56.86	58.98	71.20	74.11	50.07	83.73	74.80	45.97	59.73	54.21	40.54	64.77	56.55
U2Net [79]	55.32	72.79	65.21	47.68	80.86	65.39	42.75	58.19	49.01	34.53	61.90	52.89	58.22	80.27	63.89	57.25	76.63	71.31	45.12	57.93	52.41	42.01	63.94	54.45
PanFlowNet [80]	54.67	66.05	64.31	42.9	82.62	72.13	41.40	55.85	46.55	32.61	59.87	53.49	52.05	56.49	62.29	51.43	78.68	63.39	37.69	51.86	39.95	32.69	61.16	40.47
P2Sharpen [15]	57.19	70.45	69.37	48.47	82.49	72.36	44.49	59.12	52.80	35.49	62.61	56.91	61.32	71.86	78.90	58.68	80.77	77.69	48.47	61.98	58.31	43.81	65.11	61.63
DISPNet [81]	57.67	69.49	73.03	46.02	81.59	75.91	44.10	58.31	54.28	34.64	62.78	54.60	60.57	74.87	73.14	58.96	79.66	76.80	47.51	60.90	57.90	43.01	65.09	58.17
CANConv [82]	57.15	72.57	70.33	50.17	81.11	68.71	44.77	59.21	53.56	35.89	63.06	56.90	60.12	75.27	73.36	51.44	84.45	76.20	47.87	60.88	57.13	41.70	66.15	61.34
PAPS [83]	56.50	71.37	67.10	48.04	80.58	71.90	43.61	57.14	50.23	35.92	61.57	56.80	60.16	73.32	73.25	59.22	83.01	72.15	48.11	61.19	56.57	44.71	65.69	60.47
UniPAN [26]	57.85	69.71	70.27	48.66	82.85	75.61	44.86	58.95	53.77	35.89	63.15	57.37	61.60	73.90	80.52	54.67	80.70	79.84	48.50	61.80	58.49	43.20	65.74	61.78
WFANet [84]	56.15	71.13	66.41	46.76	79.84	72.78	42.85	56.44	47.96	35.01	62.00	55.71	59.95	72.40	74.27	57.42	82.90	72.72	47.59	60.38	55.71	44.01	65.81	59.64
CSLP [58]	58.34	73.33	74.37	51.16	80.79	70.36	45.98	60.71	56.07	37.60	63.00	58.48	61.58	75.01	77.83	59.09	82.87	74.70	49.68	62.87	60.92	45.35	66.32	62.60
DAISP [5]	55.93	71.56	66.31	50.26	81.19	66.27	43.65	57.94	51.79	34.71	62.43	55.03	58.71	80.37	68.05	53.79	77.81	72.24	46.22	57.72	54.51	40.65	64.73	59.69
FoundPS-L	59.30	74.57	71.63	54.51	80.87	74.21	46.82	60.41	56.53	40.07	63.97	59.94	62.01	74.99	76.59	61.70	82.98	75.82	50.12	62.54	61.26	47.08	66.80	63.03

TABLE XI: Segmentation performance on the SegGF dataset. **Bold** means the best average segmentation performance.

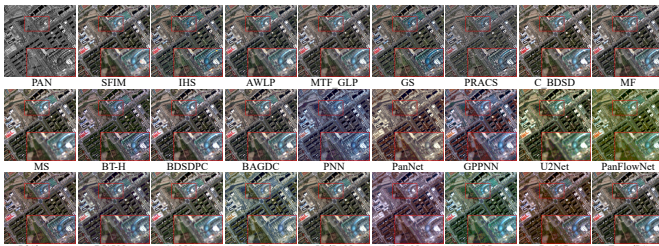


Fig. 17: Visual comparisons of full scale on SegGF.

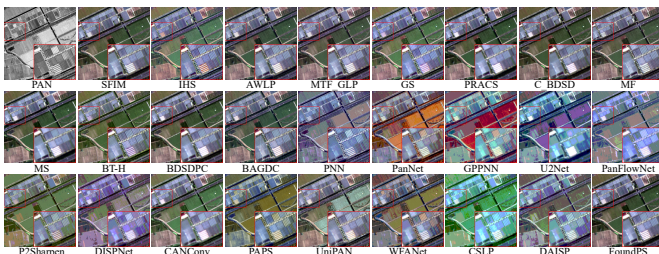


Fig. 18: Visual comparisons of full scale on Quickbird.

segmentation accuracy is significantly lower than that of lower-quality MS images, which highlights the critical influence of spectral information on segmentation. In comparison to other pansharpening methods, it is evident that the fusion of PAN and MS images can significantly enhance performance and accuracy in high-level tasks. Notably, our method achieves the best segmentation performance, particularly in highlighted regions. This demonstrates that our fusion method achieves the highest consistency between spectral and spatial information, leading to superior overall performance. Furthermore, we quantitatively evaluate the segmentation results using the

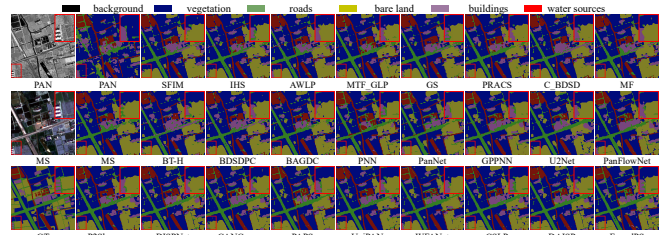


Fig. 19: Reduced-scale segmentation comparisons on SegGF.

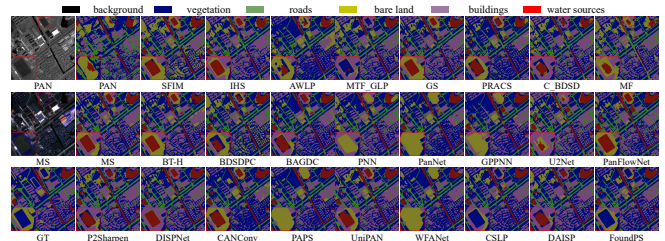


Fig. 20: Full-scale segmentation comparisons on SegGF.

intersection over Union (IoU) and accuracy (Acc.) metrics, as presented in Tab. XI. Particularly, our method has the highest mean IoU and Acc., indicating the best overall performance.

G. Remote Sensing Application

To evaluate the spectral fidelity of each pansharpening method across diverse band configurations, we systematically evaluate the effectiveness of each method in remote sensing applications by computing four key normalized difference indices using specific band combinations. Specifically, we generate the normalized difference vegetation index (NDVI) [92] in four-band datasets, water index (NDWI) [93] in seven-band

TABLE XII: Quantitative comparisons over four representative remote sensing application. The best results are shown in **bold**. The up or down arrows indicate higher or lower values correspond to better results.

Method	4 Bands (NDVI)			7 Bands (NDWI)			8 Bands (NDRE)			10 Bands (NDBI)			Average		
	RMSE↓	MAE↓	CC↑	RMSE↓	MAE↓	CC↑	RMSE↓	MAE↓	CC↑	RMSE↓	MAE↓	CC↑	RMSE↓	MAE↓	CC↑
SFIM [73]	0.1202	0.0719	0.7965	0.0326	0.0204	0.9094	0.0966	0.0536	0.6701	0.0254	0.0175	0.9250	0.0701	0.0422	0.8401
IHS [42]	0.1114	0.0748	0.8077	0.0373	0.0252	0.8802	0.0846	0.0526	0.6965	0.0257	0.0178	0.9233	0.0662	0.0440	0.8421
AWLP [45]	0.2294	0.1227	0.6739	0.0298	0.0205	0.9136	0.2563	0.1369	0.3355	0.0221	0.0150	0.9398	0.1299	0.0713	0.7539
MTF_GLP [74]	0.1353	0.0808	0.7747	0.0317	0.0189	0.9223	0.1398	0.0698	0.5704	0.0217	0.0140	0.9434	0.0803	0.0463	0.8262
GS [44]	0.1088	0.0722	0.8077	0.0432	0.0286	0.8597	0.0835	0.0503	0.6994	0.0276	0.0193	0.9209	0.0668	0.0439	0.8381
PRACS [75]	0.2377	0.1402	0.6050	0.0345	0.0222	0.8788	0.1710	0.0982	0.4921	0.0291	0.0179	0.9067	0.1233	0.0729	0.7360
C_BSDS [76]	0.1536	0.0924	0.8002	0.0274	0.0173	0.9398	0.1849	0.0982	0.5088	0.0230	0.0159	0.9520	0.0929	0.0548	0.8319
MF [77]	0.1097	0.0656	0.8204	0.0286	0.0182	0.9307	0.0850	0.0480	0.7177	0.0198	0.0141	0.9464	0.0622	0.0377	0.8662
BT-H [43]	0.1416	0.0784	0.7413	0.0264	0.0182	0.9195	0.0763	0.0438	0.7177	0.0201	0.0138	0.9469	0.0717	0.0414	0.8369
BSDSPC [8]	0.1058	0.0666	0.8528	0.0221	0.0150	0.9480	0.1025	0.0569	0.6974	0.0191	0.0147	0.9511	0.0620	0.0390	0.8791
BAGDC [50]	0.1306	0.0709	0.7944	0.0224	0.0155	0.9402	0.1694	0.0944	0.4590	0.0231	0.0168	0.9448	0.0818	0.0468	0.8202
PNN [51]	0.1409	0.1097	0.7379	0.0635	0.0462	0.6573	0.1323	0.0836	0.4035	0.0590	0.0473	0.7776	0.0990	0.0741	0.6873
PanNet [52]	0.1849	0.1539	0.7634	0.0593	0.0479	0.7796	0.1342	0.0893	0.4943	0.0594	0.0489	0.7524	0.1139	0.0911	0.7231
GPPNN [78]	0.1441	0.1109	0.7591	0.0512	0.0399	0.8160	0.1128	0.0850	0.5390	0.0403	0.0306	0.8293	0.0889	0.0681	0.7598
U2Net [79]	0.1201	0.0881	0.7842	0.0510	0.0349	0.7483	0.0801	0.0502	0.7118	0.0487	0.0377	0.7363	0.0785	0.0565	0.7515
PanFlowNet [80]	0.1093	0.0742	0.8208	0.0582	0.0405	0.7369	0.1347	0.0860	0.5070	0.0438	0.0252	0.7928	0.0825	0.0539	0.7505
P2Sharpen [15]	0.1374	0.1045	0.8311	0.0383	0.0286	0.8713	0.1283	0.0768	0.5826	0.0420	0.0323	0.8302	0.0872	0.0632	0.8014
DISPNet [81]	0.1334	0.0933	0.8263	0.0375	0.0269	0.8560	0.0893	0.0531	0.7276	0.0357	0.0286	0.9357	0.0778	0.0544	0.8529
CANConv [82]	0.1020	0.0673	0.8213	0.0458	0.0342	0.8330	0.0990	0.0561	0.6925	0.0372	0.0328	0.9463	0.0703	0.0485	0.8453
PAPS [83]	0.1284	0.0971	0.8142	0.0344	0.0251	0.8938	0.0712	0.0460	0.7570	0.0374	0.0289	0.8568	0.0734	0.0544	0.8339
UniPAN [26]	0.0968	0.0681	0.8591	0.0462	0.0332	0.8077	0.1307	0.0763	0.6004	0.0347	0.0288	0.9324	0.0724	0.0502	0.8358
WFANet [84]	0.1215	0.0932	0.7952	0.0563	0.0455	0.7425	0.0809	0.0529	0.7111	0.0285	0.0206	0.8978	0.0734	0.0550	0.8070
CSLP [58]	0.0961	0.0660	0.8671	0.0296	0.0204	0.9153	0.0770	0.0445	0.7435	0.0349	0.0276	0.8973	0.0614	0.0421	0.8674
DAISP [5]	0.1099	0.0729	0.8258	0.0342	0.0236	0.8688	0.0785	0.0464	0.7319	0.0302	0.0228	0.9272	0.0657	0.0438	0.8528
FoundPS	0.0733	0.0460	0.9022	0.0202	0.0141	0.9515	0.0613	0.0429	0.7669	0.0188	0.0131	0.9548	0.0442	0.0291	0.9083

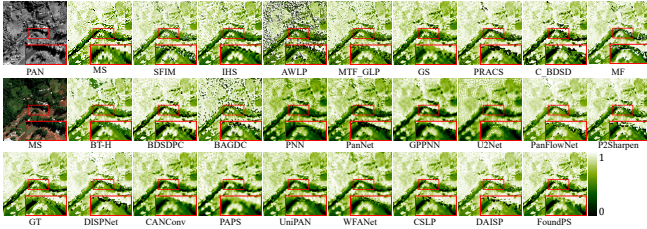


Fig. 21: Remote sensing application of NDVI.

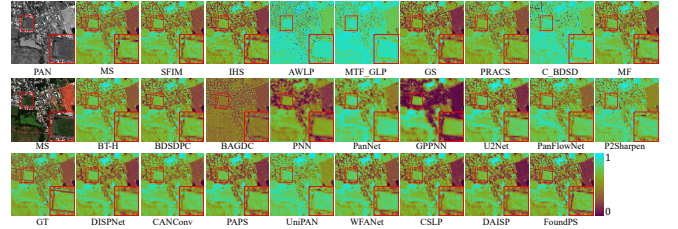


Fig. 23: Remote sensing application of NDRE.

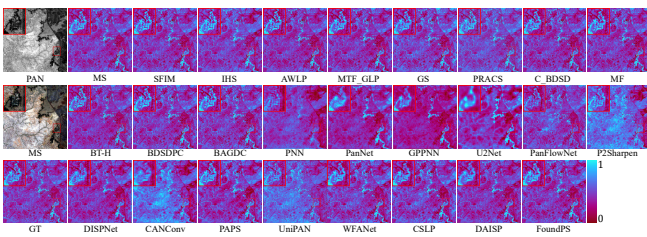


Fig. 22: Remote sensing application of NDWI.

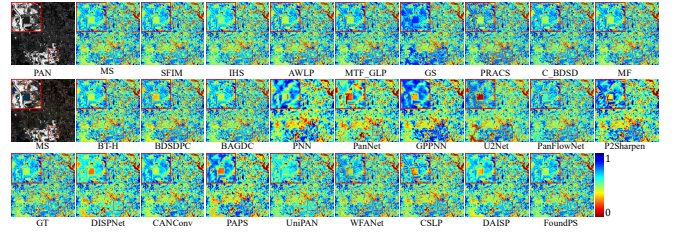


Fig. 24: Remote sensing application of NDBI.

datasets, red edge index (NDRE) [94] in eight-band datasets and building index (NDBI) [95] in ten-band datasets. Their definitions are given below:

$$\text{NDVI} = \frac{NIR - R}{NIR + R}, \quad (31)$$

$$\text{NDWI} = \frac{G - NIR}{G + NIR}, \quad (32)$$

$$\text{NDRE} = \frac{NIR - RE}{NIR + RE}, \quad (33)$$

$$\text{NDBI} = \frac{SWIR - NIR}{SWIR + NIR}, \quad (34)$$

In accordance with these definitions, the normalized difference indices are confined to the range of $[-1, 1]$, which can serve as the spectral accuracy indicators of the pansharpening process to a certain extent. The quantitative results over these four indices are presented in Tab. XII. Clearly, our method achieves the highest values across all these objective metrics, namely root mean squared error (RMSE), mean absolute error (MAE), and correlation coefficient (CC). Moreover, we present the visualizations of them in Fig. 21, Fig. 22, Fig. 23, and Fig. 24, respectively. Particularly, all of our index maps exhibit the closest resemblance to the reference, while the other methods suffer from intensity distortions.

V. CONCLUSION AND DISCUSSION

In this work, we present FoundPS, a universal foundation model for pansharpening that establishes a unified, band-agnostic, and scene-robust fusion paradigm. By projecting MS images with arbitrary band configurations into a shared latent space and performing diffusion-based cross-modal fusion, FoundPS enables a model to generalize across heterogeneous sensors and diverse scenes. To support large-scale training and fair evaluation, we further construct PSBench, a comprehensive worldwide benchmark comprising multi-satellite MS and PAN image pairs, which fills a critical gap in the development of pansharpening foundation models. Extensive experiments demonstrate that existing pansharpening methods, particularly lightweight or small-capacity models, often fail to achieve robust performance under heterogeneous spectral settings. This limitation stems not only from insufficient model capacity, but more fundamentally from the lack of architectural designs that can internalize and disentangle diverse spectral modalities within a unified representation. As a result, such models struggle to fully capture cross-band and cross-sensor characteristics, leading to degraded generalization performance on large-scale and multi-modal benchmarks.

While FoundPS provides an effective and scalable pipeline for universal pansharpening, several limitations remain. First, due to hardware constraints, the current implementation processes PAN images using patches up to 1024×1024 pixels, which limits direct modeling of ultra-large, gigapixel-scale satellite scenes. Second, the bridge posterior sampling strategy requires gradient preservation during inference, introducing additional computational and memory overhead. Finally, although FoundPS follows the foundation-model paradigm, its parameter scale remains moderate compared with extremely large generative models, as we deliberately balance model capacity against the memory usage. Addressing these limitations, especially scaling to larger contexts and improving inference efficiency, remains an important direction for future work.

REFERENCES

- [1] K. Wu, Y. Zhang, L. Ru, B. Dang, J. Lao, L. Yu, J. Luo, Z. Zhu, Y. Sun, J. Zhang *et al.*, “A semantic-enhanced multi-modal remote sensing foundation model for earth observation,” *Nat. Mach. Intell.*, vol. 7, no. 8, pp. 1235–1249, 2025.
- [2] S. Xu, Z. Zhao, H. Bai, C. Yu, J. Peng, X. Cao, and D. Meng, “Hipandas: Hyperspectral image joint denoising and super-resolution by image fusion with the panchromatic image,” in *Proc. IEEE Int. Conf. Comput. Vis.*, 2025, pp. 12 002–12 011.
- [3] M. Ciotola, G. Guarino, G. Vivone, G. Poggi, J. Chanussot, A. Plaza, and G. Scarpa, “Hyperspectral pansharpening: Critical review, tools, and future perspectives,” *IEEE Geosci. Remote Sens. Mag.*, 2024.
- [4] M. Zhou, X. He, and D. Hong, “Toward resolution mismatching: Modality-aware feature-aligned network for pan-sharpening,” *IEEE Trans. Pattern Anal. Mach. Intell.*, 2025.
- [5] H. Wang and J. Ma, “Deep adaptive unfolded network via spatial morphology stripping and spectral filtration for pan-sharpening,” in *Proc. IEEE Int. Conf. Comput. Vision*, 2025, pp. 10 730–10 740.
- [6] X. Wang, Q. Hu, Y. Cheng, and J. Ma, “Hyperspectral image super-resolution meets deep learning: A survey and perspective,” *Proc. Int. Joint Conf. Artif. Intell.*, vol. 10, no. 8, pp. 1664–1687, 2023.
- [7] S. K. Roy, G. Vivone, S. Das, B. Raman, P. Singh *et al.*, “From classical image fusion to deep representation learning: A survey of the advances in hyperspectral image pan-sharpening,” *Inf. Fusion*, p. 103834, 2025.
- [8] G. Vivone, “Robust band-dependent spatial-detail approaches for panchromatic sharpening,” *IEEE Trans. Geosci. Remote Sens.*, vol. 57, no. 9, pp. 6421–6433, 2019.
- [9] L. Alparone, S. Baronti, B. Aiazzi, and A. Garzelli, “Spatial methods for multispectral pansharpening: Multiresolution analysis demystified,” *IEEE Trans. Geosci. Remote Sens.*, vol. 54, no. 5, pp. 2563–2576, 2016.
- [10] A. Guo, R. Dian, N. Wang, and S. Li, “Better image filter for pansharpening,” *IEEE Trans. Image Process.*, vol. 34, pp. 8171–8184, 2025.
- [11] B. Zhang, Y. Wu, B. Zhao, J. Chanussot, D. Hong, J. Yao, and L. Gao, “Progress and challenges in intelligent remote sens. satellite systems,” *IEEE J. Sel. Top. Appl. Earth Obs. Remote Sens.*, vol. 15, pp. 1814–1822, 2022.
- [12] X. Fu, Z. Lin, Y. Huang, and X. Ding, “A variational pan-sharpening with local gradient constraints,” in *Proc. IEEE Conf. Comput. Vis. Pattern Recog.*, 2019, pp. 10 265–10 274.
- [13] S. Ruder, “An overview of gradient descent optimization algorithms,” *arXiv preprint arXiv:1609.04747*, 2016.
- [14] K. Zhang, F. Zhang, W. Wan, H. Yu, J. Sun, J. Del Ser, E. Elyan, and A. Hussain, “Panchromatic and multispectral image fusion for remote sens. and earth observation: Concepts, taxonomy, literature review, evaluation methodologies and challenges ahead,” *Inf. Fusion*, vol. 93, pp. 227–242, 2023.
- [15] H. Zhang, H. Wang, X. Tian, and J. Ma, “P2sharpen: A progressive pansharpening network with deep spectral transformation,” *Inf. Fusion*, vol. 91, pp. 103–122, 2023.
- [16] J. Wang, Y. Lin, C. Chen, X. Huang, R. Zhang, Y. Wang, and T. Lu, “From forgotten to pan-sharpening,” *Pattern Recog.*, p. 112653, 2025.
- [17] Q. Xu, Y. Li, J. Nie, Q. Liu, and M. Guo, “Upangan: Unsupervised pansharpening based on the spectral and spatial loss constrained generative adversarial network,” *Inf. Fusion*, vol. 91, pp. 31–46, 2023.
- [18] Y. Shang, J. Liu, J. Zhang, and Z. Wu, “Mft-gan: A multiscale feature-guided transformer network for unsupervised hyperspectral pansharpening,” *IEEE Trans. Geosci. Remote Sens.*, vol. 62, pp. 1–16, 2024.
- [19] J. Hou, Z. Cao, N. Zheng, X. Li, X. Chen, X. Liu, X. Cong, D. Hong, and M. Zhou, “Linearly-evolved transformer for pan-sharpening,” in *Proc. ACM Int. Conf. Multimed.*, 2024, pp. 1486–1494.
- [20] L. He, H. Ye, J. Li, and A. Plaza, “Transformer-ensemble based implicit spectral-spatial functions for arbitrary-resolution hyperspectral pansharpening,” *IEEE Trans. Geosci. Remote Sens.*, 2025.
- [21] X. He, K. Cao, J. Zhang, K. Yan, Y. Wang, R. Li, C. Xie, D. Hong, and M. Zhou, “Pan-mamba: Effective pan-sharpening with state space model,” *Inf. Fusion*, vol. 115, p. 102779, 2025.
- [22] S. Hou, S. Xiao, J. Qu, and W. Dong, “Mambamt: Progressive mutual-guided mamba multi-task learning for hyperspectral image pansharpening and classification,” *IEEE Trans. Geosci. Remote Sens.*, 2025.
- [23] H. Wang, H. Zhang, X. Tian, and J. Ma, “Zero-sharpen: A universal pansharpening method across satellites for reducing scale-variance gap via zero-shot variation,” *Inf. Fusion*, vol. 101, p. 102003, 2024.
- [24] J.-L. Xiao, T.-Z. Huang, L.-J. Deng, G. Lin, Z. Cao, C. Li, and Q. Zhao, “Hyperspectral pansharpening via diffusion models with iteratively zero-shot guidance,” in *Proc. IEEE Conf. Comput. Vis. Pattern Recog.*, 2025, pp. 12 669–12 678.
- [25] Q. Cao, L.-J. Deng, W. Wang, J. Hou, and G. Vivone, “Zero-shot semi-supervised learning for pansharpening,” *Inf. Fusion*, vol. 101, p. 102001, 2024.
- [26] Y. Cui, P. Liu, and H. Zhang, “Empowering your pansharpening models with generalizability: Unified distribution is all you need,” in *Proc. IEEE Int. Conf. Comput. Vision*, 2025, pp. 11 850–11 860.
- [27] R. Zhang, X. He, L. Xueheng, K. Cao, L. Liu, W. Xu, F. Jiabin, Y. Qize, and J. Zhang, “Rethinking pan-sharpening: A new training process for full-resolution generalization,” *arXiv preprint arXiv:2507.15059*, 2025.
- [28] W. Cai, J. Jiang, F. Wang, J. Tang, S. Kim, and J. Huang, “A survey on mixture of experts in large language models,” *IEEE Trans. Knowl. Data Eng.*, 2025.
- [29] Y. Xu, J. Zhang, Q. Zhang, and D. Tao, “Vitpose++: Vision transformer for generic body pose estimation,” *IEEE Trans. Pattern Anal. Mach. Intell.*, vol. 46, no. 2, pp. 1212–1230, 2023.
- [30] X. Nie, X. Miao, S. Cao, L. Ma, Q. Liu, J. Xue, Y. Miao, Y. Liu, Z. Yang, and B. Cui, “EvoMoe: An evolutionary mixture-of-experts training framework via dense-to-sparse gate,” *arXiv preprint arXiv:2112.14397*, 2021.
- [31] X. Wu, S. Huang, and F. Wei, “Mixture of lora experts,” in *Int. Conf. Learn. Represent.*
- [32] B. Pan, Y. Shen, H. Liu, M. Mishra, G. Zhang, A. Oliva, C. Raffel, and R. Panda, “Dense training, sparse inference: Rethinking training of mixture-of-experts language models,” *arXiv preprint arXiv:2404.05567*, 2024.
- [33] S. Rajbhandari, C. Li, Z. Yao, M. Zhang, R. Y. Aminabadi, A. A. Awan, J. Rasley, and Y. He, “DeepSpeed-MoE: Advancing mixture-of-experts inference and training to power next-generation ai scale,” in *Proc. Int. Conf. Mach. Learn.* PMLR, 2022, pp. 18 332–18 346.

- [34] T. Wei, B. Zhu, L. Zhao, C. Cheng, B. Li, W. Lü, P. Cheng, J. Zhang, X. Zhang, L. Zeng *et al.*, “Skywork-moe: A deep dive into training techniques for mixture-of-experts language models,” *arXiv preprint arXiv:2406.06563*, 2024.
- [35] M. Lewis, S. Bhosale, T. Dettmers, N. Goyal, and L. Zettlemoyer, “Base layers: Simplifying training of large, sparse models,” in *Proc. Int. Conf. Mach. Learn.* PMLR, 2021, pp. 6265–6274.
- [36] A. Q. Jiang, A. Sablayrolles, A. Roux, A. Mensch, B. Savary, C. Bamford, D. S. Chaplot, D. d. I. Casas, E. B. Hanna, F. Bressand *et al.*, “Mixtral of experts,” *arXiv preprint arXiv:2401.04088*, 2024.
- [37] B. Lenz, O. Lieber, A. Arazi, A. Bergman, A. Manevich, B. Peleg, B. Aviram, C. Almagor, C. Fridman, D. Padnos *et al.*, “Jamba: Hybrid transformer-mamba language models,” in *Int. Conf. Learn. Represent.*, 2025.
- [38] S. Wu, J. Luo, X. Chen, L. Li, X. Zhao, T. Yu, C. Wang, Y. Wang, F. Wang, W. Qiao *et al.*, “Yuan 2.0-m32: Mixture of experts with attention router,” *arXiv preprint arXiv:2405.17976*, 2024.
- [39] X. Ren, P. Zhou, X. Meng, S. Huang, Y. Wang, W. Wang, P. Li, X. Zhang, A. Podolskiy, G. Arshinov *et al.*, “Pangu- $\{\Sigma\}$: Towards trillion parameter language model with sparse heterogeneous computing,” *arXiv preprint arXiv:2303.10845*, 2023.
- [40] A. Wang, X. Sun, R. Xie, S. Li, J. Zhu, Z. Yang, P. Zhao, W. Han, Z. Kang, D. Wang *et al.*, “Hmoe: Heterogeneous mixture of experts for language modeling,” in *Proc. Conf. Empir. Methods Nat. Lang. Process.*, 2025, pp. 21954–21968.
- [41] Y. Li, S. Jiang, B. Hu, L. Wang, W. Zhong, W. Luo, L. Ma, and M. Zhang, “Uni-moe: Scaling unified multimodal llms with mixture of experts,” *IEEE Trans. Pattern Anal. Mach. Intell.*, 2025.
- [42] T.-M. Tu, S.-C. Su, H.-C. Shyu, and P. S. Huang, “A new look at ihs-like image fusion methods,” *Inf. Fusion*, vol. 2, no. 3, pp. 177–186, 2001.
- [43] S. Lolli, L. Alparone, A. Garzelli, and G. Vivone, “Haze correction for contrast-based multispectral pansharpening,” *IEEE Geosci. Remote Sens. Lett.*, vol. 14, no. 12, pp. 2255–2259, 2017.
- [44] B. Aiazzi, S. Baronti, and M. Selva, “Improving component substitution pansharpening through multivariate regression of ms + pan data,” *IEEE Trans. Geosci. Remote Sens.*, vol. 45, no. 10, pp. 3230–3239, 2007.
- [45] X. Otazu, M. González-Audicana, O. Fors, and J. Núñez, “Introduction of sensor spectral response into image fusion methods. application to wavelet-based methods,” *IEEE Trans. Geosci. Remote Sens.*, vol. 43, no. 10, pp. 2376–2385, 2005.
- [46] M. Pradeep, “Implementation of image fusion algorithm using matlab (laplacian pyramid),” in *Proc. Int. Multi-Conf. Autom. Comput. Commun. Control Compress. Sens.* IEEE, 2013, pp. 165–168.
- [47] G. Vivone, L. Alparone, J. Chanussot, M. Dalla Mura, A. Garzelli, G. A. Licciardi, R. Restaino, and L. Wald, “A critical comparison among pansharpening algorithms,” *IEEE Trans. Geosci. Remote Sens.*, vol. 53, no. 5, pp. 2565–2586, 2014.
- [48] C. Ballester, V. Caselles, L. Igual, J. Verdera, and B. Rougé, “A variational model for p+ xs image fusion,” *Int. J. Comput. Vis.*, vol. 69, no. 1, pp. 43–58, 2006.
- [49] C. Chen, Y. Li, W. Liu, and J. Huang, “Sirf: Simultaneous satellite image registration and fusion in a unified framework,” *IEEE Trans. Image Process.*, vol. 24, no. 11, pp. 4213–4224, 2015.
- [50] H. Lu, Y. Yang, S. Huang, W. Tu, and W. Wan, “A unified pansharpening model based on band-adaptive gradient and detail correction,” *IEEE Trans. Image Process.*, vol. 31, pp. 918–933, 2021.
- [51] G. Masi, D. Cozzolino, L. Verdoliva, and G. Scarpa, “Pansharpening by convolutional neural networks,” *Remote Sens.*, vol. 8, no. 7, p. 594, 2016.
- [52] J. Yang, X. Fu, Y. Hu, Y. Huang, X. Ding, and J. Paisley, “Pannet: A deep network architecture for pan-sharpening,” in *Proc. IEEE Int. Conf. Comput. Vision*, 2017, pp. 5449–5457.
- [53] H. Zhou, Q. Liu, and Y. Wang, “Panformer: A transformer based model for pan-sharpening,” in *Int. Conf. Multimedia and Expo.* IEEE, 2022, pp. 1–6.
- [54] X. He, K. Cao, J. Zhang, K. Yan, Y. Wang, R. Li, C. Xie, D. Hong, and M. Zhou, “Pan-mamba: Effective pan-sharpening with state space model,” *Inf. Fusion*, p. 102779, 2024.
- [55] Z. Cao, S. Cao, L.-J. Deng, X. Wu, J. Hou, and G. Vivone, “Diffusion model with disentangled modulations for sharpening multispectral and hyperspectral images,” *Inf. Fusion*, vol. 104, p. 102158, 2024.
- [56] M. Zhou, J. Huang, K. Yan, D. Hong, X. Jia, J. Chanussot, and C. Li, “A general spatial-frequency learning framework for multimodal image fusion,” *IEEE Trans. Pattern Anal. Mach. Intell.*, 2024.
- [57] M. Ma, Y. Jiang, M. Zhao, X. Ma, W. Zhang, and S. Song, “Deep spatial-spectral fusion transformer for remote sens. pansharpening,” *Inf. Fusion*, vol. 118, p. 102980, 2025.
- [58] Y. Chen, Z. Wan, Z. Chen, and M. Wei, “Cslp: A novel pansharpening method based on compressed sensing and l-pnn,” *Inf. Fusion*, vol. 118, p. 103002, 2025.
- [59] D. Li, C. Luo, Y. Bao, G. Yang, J. Xiao, X. Fu, and Z.-J. Zha, “Enhanced pansharpening via quaternion spatial-spectral interactions,” in *Proc. IEEE Conf. Comput. Vis. Pattern Recogn.*, 2025, pp. 10908–10918.
- [60] J. Hu, P. Hu, X. Kang, H. Zhang, and S. Fan, “Pan-sharpening via multiscale dynamic convolutional neural network,” *IEEE Trans. Geosci. Remote Sens.*, vol. 59, no. 3, pp. 2231–2244, 2020.
- [61] G. Yang, M. Zhou, K. Yan, A. Liu, X. Fu, and F. Wang, “Memory-augmented deep conditional unfolding network for pan-sharpening,” in *Proc. IEEE Conf. Comput. Vis. Pattern Recogn.*, 2022, pp. 1788–1797.
- [62] J. Ma, W. Yu, C. Chen, P. Liang, X. Guo, and J. Jiang, “Pan-gan: An unsupervised pan-sharpening method for remote sens. image fusion,” *Inf. Fusion*, vol. 62, pp. 110–120, 2020.
- [63] Y. Zhong, X. Wu, Z. Cao, H.-X. Dou, and L.-J. Deng, “Ssdiff: Spatial-spectral integrated diffusion model for remote sens. pansharpening,” *Adv. Neural Inform. Process. Syst.*, vol. 37, pp. 77962–77986, 2024.
- [64] Y. Cui, P. Liu, and Y. Zeng, “Leveraging large-scale pretrained spatial-spectral priors for general zero-shot pansharpening,” *arXiv preprint arXiv:2512.02643*, 2025.
- [65] L. Wald, T. Ranchin, and M. Mangolini, “Fusion of satellite images of different spatial resolutions: Assessing the quality of resulting images,” *Photogramm. Eng. Remote Sens.*, vol. 63, no. 6, pp. 691–699, 1997.
- [66] K. Han, Y. Wang, H. Chen, X. Chen, J. Guo, Z. Liu, Y. Tang, A. Xiao, C. Xu, Y. Xu *et al.*, “A survey on vision transformer,” *IEEE Trans. Pattern Anal. Mach. Intell.*, vol. 45, no. 1, pp. 87–110, 2022.
- [67] D. Kieu, K. Do, T. Nguyen, D. Nguyen, and T. Nguyen, “Bidirectional diffusion bridge models,” in *Proc. ACM SIGKDD Int. Conf. Knowl. Discov. Data Min.*, 2025, pp. 1139–1148.
- [68] H. Wang, J. Zhang, H. Chen, H. Guo, D. Wang, J. Ma, and B. Du, “Residual diffusion bridge model for image restoration,” *arXiv preprint arXiv:2512.02643*, 2025.
- [69] B. Efron, “Tweedie’s formula and selection bias,” *J. Am. Stat. Assoc.*, vol. 106, no. 496, pp. 1602–1614, 2011.
- [70] H. Chung, J. Kim, M. T. McCann, M. L. Klasky, and J. C. Ye, “Diffusion posterior sampling for general noisy inverse problems,” in *Int. Conf. Learn. Represent.*, 2023.
- [71] T. Li and K. He, “Back to basics: Let denoising generative models denoise,” *arXiv preprint arXiv:2511.13720*, 2025.
- [72] X. Ma, X. Dai, Y. Bai, Y. Wang, and Y. Fu, “Rewrite the stars,” in *Proc. IEEE Conf. Comput. Vis. Pattern Recogn.*, 2024, pp. 5694–5703.
- [73] J. Liu, “Smoothing filter-based intensity modulation: A spectral preserve image fusion technique for improving spatial details,” *Int. J. Remote Sens.*, vol. 21, no. 18, pp. 3461–3472, 2000.
- [74] B. Aiazzi, L. Alparone, S. Baronti, A. Garzelli, and M. Selva, “Mtf-tailored multiscale fusion of high-resolution ms and pan imagery,” *Photogramm. Eng. Remote Sens.*, vol. 72, no. 5, pp. 591–596, 2006.
- [75] J. Choi, K. Yu, and Y. Kim, “A new adaptive component-substitution-based satellite image fusion by using partial replacement,” *IEEE Trans. Geosci. Remote Sens.*, vol. 49, no. 1, pp. 295–309, 2010.
- [76] A. Garzelli, “Pansharpening of multispectral images based on nonlocal parameter optimization,” *IEEE Trans. Geosci. Remote Sens.*, vol. 53, no. 4, pp. 2096–2107, 2014.
- [77] R. Restaino, G. Vivone, M. Dalla Mura, and J. Chanussot, “Fusion of multispectral and panchromatic images based on morphological operators,” *IEEE Trans. Image Process.*, vol. 25, no. 6, pp. 2882–2895, 2016.
- [78] S. Xu, J. Zhang, Z. Zhao, K. Sun, J. Liu, and C. Zhang, “Deep gradient projection networks for pan-sharpening,” in *Proc. IEEE Conf. Comput. Vis. Pattern Recogn.*, 2021, pp. 1366–1375.
- [79] S. Peng, C. Guo, X. Wu, and L.-J. Deng, “U2net: A general framework with spatial-spectral-integrated double u-net for image fusion,” in *Proc. ACM Int. Conf. Multimed.*, 2023, pp. 3219–3227.
- [80] G. Yang, X. Cao, W. Xiao, M. Zhou, A. Liu, X. Chen, and D. Meng, “Panflownet: A flow-based deep network for pan-sharpening,” in *Proc. IEEE Conf. Comput. Vis. Pattern Recogn.*, 2023, pp. 16857–16867.
- [81] H. Wang, M. Gong, X. Mei, H. Zhang, and J. Ma, “Deep unfolded network with intrinsic supervision for pan-sharpening,” in *Proc. AAAI Conf. Artif. Intell.*, vol. 38, no. 6, 2024, pp. 5419–5426.
- [82] Y. Duan, X. Wu, H. Deng, and L.-J. Deng, “Content-adaptive non-local convolution for remote sens. pansharpening,” in *Proc. IEEE Conf. Comput. Vis. Pattern Recogn.*, 2024, pp. 27738–27747.
- [83] Y. Jia, Q. Hu, R. Dian, J. Ma, and X. Guo, “Paps: Progressive attention-based pan-sharpening,” *IEEE CAA J. Autom. Sin.*, vol. 11, no. 2, pp. 391–404, 2024.

- [84] J. Huang, R. Huang, J. Xu, S. Peng, Y. Duan, and L.-J. Deng, "Wavelet-assisted multi-frequency attention network for pansharpening," in *Proc. AAAI Conf. Artif. Intell.*, vol. 39, no. 4, 2025, pp. 3662–3670.
- [85] Q. Huynh-Thu and M. Ghanbari, "Scope of validity of psnr in image/video quality assessment," *Electron. Lett.*, vol. 44, no. 13, pp. 800–801, 2008.
- [86] Z. Wang, A. C. Bovik, H. R. Sheikh, and E. P. Simoncelli, "Image quality assessment: from error visibility to structural similarity," *IEEE Trans. Image Process.*, vol. 13, no. 4, pp. 600–612, 2004.
- [87] L. Wald, *Data fusion: definitions and architectures: fusion of images of different spatial resolutions*. Presses des MINES, 2002.
- [88] L. Alparone, L. Wald, J. Chanussot, C. Thomas, P. Gamba, and L. M. Bruce, "Comparison of pansharpening algorithms: Outcome of the 2006 grs-s data-fusion contest," *IEEE Trans. Geosci. Remote. Sens.*, vol. 45, no. 10, pp. 3012–3021, 2007.
- [89] L. Alparone, B. Aiazzi, S. Baronti, A. Garzelli, F. Nencini, and M. Selva, "Multispectral and panchromatic data fusion assessment without reference," *Photogramm. Eng. Remote Sens.*, vol. 74, no. 2, pp. 193–200, 2008.
- [90] J. Long, E. Shelhamer, and T. Darrell, "Fully convolutional networks for semantic segmentation," in *Proc. IEEE Conf. Comput. Vis. Pattern Recogn.*, 2015, pp. 3431–3440.
- [91] E. Xie, W. Wang, Z. Yu, A. Anandkumar, J. M. Alvarez, and P. Luo, "Segformer: Simple and efficient design for semantic segmentation with transformers," *Adv. Neural Inform. Process. Syst.*, vol. 34, pp. 12 077–12 090, 2021.
- [92] C. J. Tucker, "Red and photographic infrared linear combinations for monitoring vegetation," *Remote Sens. Environ.*, vol. 8, no. 2, pp. 127–150, 1979.
- [93] S. K. McFeeters, "The use of the normalized difference water index (ndwi) in the delineation of open water features," *Int. J. Remote Sens.*, vol. 17, no. 7, pp. 1425–1432, 1996.
- [94] E. Barnes, T. Clarke, S. Richards, P. Colaizzi, J. Haberland, M. Kostrzewski, P. Waller, C. Choi, E. Riley, T. Thompson *et al.*, "Coincident detection of crop water stress, nitrogen status and canopy density using ground based multispectral data," in *Proc. Int. Conf. on Precision Agriculture*, vol. 1619, no. 6, 2000.
- [95] Y. Zha, J. Gao, and S. Ni, "Use of normalized difference built-up index in automatically mapping urban areas from tm imagery," *Int. J. Remote Sens.*, vol. 24, no. 3, pp. 583–594, 2003.